MEASUREMENT OF THE RATIO

$$\frac{BR(B^+ \to J/\psi K^+)}{BR(B^0 \to J/\psi K^0)}$$

AT THE COLLIDER DETECTOR AT FERMILAB

Julio B. González-Atavales

A DISSERTATION

in

PHYSICS

Presented to the Graduate Faculty of the University of Pennsylvania in Partial

Fulfillment of the Requirements for the Degree of Doctor of Philosophy

1995

Supervisor of Dissertation

Graduate Group Chairman

ACKNOWLEDGMENTS

It is seven years later and it seems I am finally shedding the investiture of a student to reach the next stage in my life. This perilous trip has been completed with much needed help from many people. First I acknowledge the guidance of my advisor Professor Nigel Lockyer. He was always available when I needed his help, support, and experience. He also provided an atmosphere of comradeship and trust that allowed me to endure the times when hopelessness seemed to be entrenched all around. His help in the process of getting this analysis approved and getting this thesis well written has been enormous. I am also grateful for all the help in this analysis that I received from Dr. Joel Heinrich. His technical expertise allowed me to do a much better job. I usually get the impression that Joel knows everything and that he is always willing to explain things very carefully. I also must thank him for carefully proof-reading my earlier version in order to bring my writing to resemble the english language.

I also thank Professor Eugene Beier, who as chairman of my thesis committee, provided comments and suggestions.

I would also like to thank the help received from so many people here at Penn and at CDF.

ABSTRACT

MEASUREMENT OF THE RATIO $\frac{BR(B^+ \to J/\psi K^+)}{BR(B^0 \to J/\psi K^0)}$ AT THE COLLIDER DETECTOR AT FERMILAB

Julio B. González-Atavales

Nigel S. Lockyer

We report on the first reconstruction of the decay mode $B^0(\bar{B}^0) \to J/\psi K^0_S$ in a hadronic environment. The data were obtained at the Collider Detector at Fermilab (CDF) in $\bar{p}p$ collisions at $\sqrt{s} = 1.8$ TeV. The resulting $J/\psi K^0_S$ signal consists of 36 ± 6.4 events with a signal-to-noise ratio of 11. We also reconstruct the decay modes $B^\pm \to J/\psi K^\pm$ and $B^\pm \to J/\psi K^{*\pm}$. Assuming identical production rates for B^+ and B^0 mesons we measure the ratio of branching ratios $BR(B^+ \to J/\psi K^+)/BR(B^0 \to J/\psi K^0) = 0.88 \pm 0.18$ (stat.) ± 0.06 (sys.). This ratio provides an indirect measurement of the ratio of lifetimes $\tau(B^+)/\tau(B^0)$. We also use the value $BR(B^+ \to J/\psi K^+) = 0.110 \pm 0.015$ (stat.) $\pm$ 0.09 (sys.)% reported by the CLEO collaboration to obtain $BR(B^0 \to J/\psi K^0) = 0.125 \pm 0.031$ (stat.) $\pm$ 0.014 (sys.)%. This is the first measurement of a branching ratio in the b-quark system at CDF. The statistical significance of this result is similar to the significance of a previous result by the CLEO collaboration. We compare the ratio of branching ratios measurement and the branching ratio result to recent values from other experiments and theoretical

predictions.

Contents

1 Introduction **1**

1.1 A Brief History and Status of Beauty 2

1.2 Theoretical Context 5

2 THE COLLIDER DETECTOR AT FERMILAB **11**

2.1 The Tevatron at Fermilab 14

2.2 The Central Tracking Chamber (CTC) 16

2.3 The Vertex Time Projection Chamber (VTX) 18

2.4 The Silicon Vertex Detector (SVX) 18

2.5 The Central Muon System (CMU) 21

2.6 The Central Muon Upgrade (CMP) 23

2.7 The Central Muon Extension (CMX) 24

3 TRACKING AT CDF **25**

3.1 CTC Tracking 25

3.1.1 General Scheme 26

3.1.2 Tracking Algorithms 27

3.2 SVX Tracking 31

4 DATA SAMPLE **32**

4.1 J/ψ Trigger 32

4.2 Offline Production 33

4.3 J/ψ Candidate Events 33

5 B MESON RECONSTRUCTION **36**

5.1 Track Selection 36

5.1.1 SVX Track Selection for K_S^0 Reconstruction 37

5.1.2 SVX Track Selection for Other Tracks 41

5.2 Improving the Tracking Resolution 42

5.2.1 Constraints for the $J/\psi K^{\pm}$ Mode 43

5.2.2 Constraints for the $J/\psi K_S^0$ Mode 44

5.3 Kaon Selection 44

5.4 Combinatoric Background Reduction 45

5.5 $B^{\pm} \to J/\psi K^{*\pm}$ Decay Mode 49

5.6 $B^{\pm} \to J/\psi K^{\pm}$ and $B^0(\bar{B}^0) \to J/\psi K_S^0$ Modes 50

6 MEASURING THE RATIO OF BRANCHING RATIOS **55**

6.1 Method 55

6.2 Determining the Number of Observed Events 56

7 CTC TRACKING EFFICIENCY **60**

7.1 Method 61

7.2 Efficiency Definition 62

7.3 Tracking Efficiency Results for $J/\psi K^{\pm}$ Mode 64

7.3.1 Systematic Effects for the $J/\psi K^{\pm}$ Mode 67

7.3.2 Tracking Efficiency for the $J/\psi K^{\pm}$ Mode 67

7.4 Tracking Efficiency Results for the $J/\psi K_S^0$ Mode 69

7.4.1 Systematic Effect for the $J/\psi K_S^0$ Mode 70

7.4.2 Tracking Efficiency for the $J/\psi K_S^0$ Mode 72

8 RECONSTRUCTION EFFICIENCIES **73**

8.1 Monte Carlo Event Generator 73

8.2 Monte Carlo Sample 74

8.3 J/ψ Trigger Simulation 74

8.4 $J/\psi K^{\pm}$ Efficiency 75

8.5 $J/\psi K_S^0$ Efficiency 77

9 Systematic Uncertainties **83**

9.1 $c\tau(B)$ cut 83

9.2 Tracking Efficiency 84

9.3 Monte Carlo $P_T(b)$ Spectrum 84

9.4 Trigger Systematics 85

9.5 Pion Impact Cut 87

9.6 P_T Dependence of the Probability Cut 88

9.7 Dependence on P_T Cuts 89

9.8 Fitting Procedure 92

9.8.1 Integrate Across the Bin 92

9.8.2 Float the Width of the Gaussian 92

9.8.3 Results 94

9.9 Cancellation of Prob($\Delta\chi^2_F$) > 0.01 96

9.10 Summary of Systematics 98

10 RESULTS AND CONCLUSIONS **99**

10.1 Comparison to other $\tau(B^+)/\tau(B^0)$ Measurements and Theory 100

10.2 Comparison to Other Exclusive Branching Ratio Measurements and Theory 101

10.3 Future Prospects 103

A CP VIOLATION **109**

A.1 CKM Matrix 111

A.2 The Unitarity Triangle 114

A.3 B^0-$\bar{B}^0$ Mixing 114

A.4 Classes of CP Violation 116

A.5 CP Violation in the $J/\psi K_S^0$ Mode 117

B CDF TRACK MODEL **120**

B.1 Derivation of Track Equations 120

B.2 Track Momentum at the Vertex 123

B.3 Helix Parameters from GENP 124

B.4 Exit Radius (R_E) 127

B.5 Charged Particle Decay Vertex 129

C ROTATING A VECTOR **132**

BIBLIOGRAPHY **135**

List of Tables

5.1 The effect of different SVX track selection algorithms 41

6.1 Number of fitted events for $J/\psi K_S^0$ and $J/\psi K^\pm$ 57

7.1 List of simulated decays for the $K^\pm$ 68

8.1 Efficiencies for the $J/\psi K^\pm$ mode 82

8.2 Efficiencies for the $J/\psi K_S^0$ mode 82

9.1 Effect of maximal $P_T(B)$ shape variations 85

9.2 Efficiency of $d_\pi/\sigma_{d_\pi} > 2$ cut for different values of $P_T(K_S^0)$ 88

9.3 Study of $P_T(\pi)$ dependence of the efficiency of the Prob($\Delta\chi^2_F$) > 0.01 cut for the vertex constraint 89

9.4 Study of $P_T(\pi)$ dependence of the efficiency of the Prob($\Delta\chi^2_F$) > 0.01 cut for the mass constraint 89

9.5 Dependence of the BR/BR on the $P_T(B)$ and Kaon P_T cuts 91

9.6 Dependence of the ratio of observed events with the fitting procedure 94

9.7 Systematics of this measurement 98

10.1 A summary of recent Ratio of lifetimes measurements 101

10.2 Branching ratios measurement available at the moment for the exclusive decay channels 102

10.3 Sources of uncertainties for the ratio of branching ratio measurement 104

List of Figures

1.1 Two diagrams contributing to the decay modes $B^+(B^0) \to J/\psi K^+(K^0)$ 7

1.2 Exchange diagram for B^0 decays 8

2.1 Isometric view of the CDF detector 12

2.2 A cut-away view through the forward half of CDF 13

2.3 Layout of the Fermilab Tevatron 14

2.4 End view of the Central Tracking Chamber 17

2.5 An isometric view of one of the SVX barrels 20

2.6 Location of the central muon chambers 22

2.7 Cross section of a single muon chamber 23

3.1 Geometry for test used to link segments across superlayers 30

4.1 Distribution of $M(\mu^+\mu^-)$ for J/ψ candidate events 35

5.1 Normalized mass distribution for K_S^0 candidates showing the presence and effect of spurious SVX hits 38

5.2 Distribution of $M(\pi^+\pi^-)$ for K_S^0 candidates used in the B^0 reconstruction 46

5.3 Distribution of pseudo-$c\tau$ for the J/ψ sample with both muons in the SVX. 48

5.4 Mass distribution for $J/\psi K^{*\pm}$ decay mode 51

5.5 Mass distribution for $J/\psi K_S^0$ decay mode 53

5.6 Mass distribution for $J/\psi K^{\pm}$ decay mode 54

6.1 Normalized mass distribution for $J/\psi K_S^0$ decay mode 58

6.2 Normalized mass distribution for $J/\psi K^{\pm}$ decay mode 59

7.1 Tracking efficiency for embedded $K^{\pm}$ tracks. The $K^{\pm}$'s are not allowed to decay 65

7.2 Tracking efficiency for embedded $K^{\pm}$ tracks. The $K^{\pm}$'s are allowed to decay 66

7.3 Tracking efficiency as a function of d_0 69

7.4 Tracking efficiency as a function of $P_T(\pi)$ 70

7.5 Reconstructed B mass peak 71

8.1 Distribution of $M(\pi^+\pi^-)$ used to measure the efficiency of the $d_\pi/\sigma_{d_\pi} >$ 2 cut 79

9.1 Maximal variations of the default $P_T(b)$ spectrum used in this analysis 86

9.2 Fit using function $\tilde{f}$ -described in the text 93

9.3 Fit with a floating width 95

9.4 Distribution of $\Delta\chi^2_F$ when the $K^{\pm}$ is added or when the K_S^0 is point constrained in 3-D 97

10.1 Mass plot for $J/\psi K_S^0$ mode showing 55 ± 9 events 105

A.1 Unitarity triangle 115

A.2 Two contributions to the total decay amplitude of a neutral B meson 117

B.1 Track of a charged particle through CDF's magnetic field region . . . 121

You've asked me

What the lobster

is weaving there

with its golden feet ?

I reply

the ocean knows this.

You said

What is the ascidian waiting for,

in its transparent bell ?

What is it waiting for ?

I tell you,

it is waiting for time

like you.

by Pablo Neruda

translated by

Robert Bly

Chapter 1

Introduction

This thesis describes the first reconstruction of the decay mode $B^0(\bar{B}^0) \to J/\psi K^0_S$ in a hadronic environment. We also reconstruct the decay modes $B^\pm \to J/\psi K^\pm$ and $B^\pm \to J/\psi K^{*\pm}$. The data were obtained at the Collider Detector at Fermilab (CDF) in $\bar{p}p$ collisions at $\sqrt{s} = 1.8$ TeV during the 1992-93 run (Run-Ia). An important quantity defined for unstable particles is the branching ratio, which is the probability that a given particle will decay into a particular final state. Using the reconstructed $J/\psi K^0_S$ and $J/\psi K^\pm$ modes we make a measurement of the ratio of branching ratios $BR(B^+ \to J/\psi K^+)/BR(B^0 \to J/\psi K^0)$. The K^0 is an admixture of 50% K^0_S and 50% K^0_L. The K^0_L cannot be reconstructed at CDF, so the K^0 signal is inferred from the observed $J/\psi K^0_S$ signal. By using isospin invariance, the ratio of branching ratios is shown to correspond to the ratio of lifetimes $\tau(B^+)/\tau(B^0)$, which is an important quantity to test the present understanding of the b-quark system. Our measurement of $BR(B^+ \to J/\psi K^+)/BR(B^0 \to J/\psi K^0)$ together with the $BR(B^+ \to J/\psi K^+)$

measured by the CLEO collaboration (CLEO) can be used to calculate $BR(B^0 \to J/\psi K^0)$. The statistical significance of this result is similar to the significance of a previous result by the CLEO collaboration. This is the first time a branching ratio has been measured in the b-quark system at CDF.

In this Chapter we will first point out some landmarks in the development of b-physics and then give a brief summary of how our measurement relates to the main theoretical issues presently discussed in the study of b-physics.

1.1 A Brief History and Status of Beauty

The first evidence of the existence of a quark from a third generation came from the discovery in 1977 of a narrow resonance in the mass region 9.5-10.5 GeV/c^2 by Lederman *et al.* at Fermilab. The resonance was observed in the mass spectrum of muon pairs produced in the process p + nucleus $\to \mu^+\mu^- + X$. A year later these results were confirmed in e^+e^- experiments at the DORIS storage ring in Hamburg. The important $\Upsilon(4S)$ was first observed in e^+e^- collisions at CESR at Cornell in 1980. The mass of this state ($\sim$ 10.6 GeV/c^2) is approximately 20 MeV/c^2 above the threshold for open beauty production, meaning this state is the first $b\bar{b}$ resonance which can decay into $B\bar{B}$ mesons, each containing a b-quark. Since then CESR has accumulated high statistics at the $\Upsilon(4S)$, which is currently the principal source of information on B decays.

The discovery of the b-quark had been predated by some theoretical analysis which predicted a third generation of quarks. The third-family lepton (τ) had already been discovered in 1975, predicting (via the assumption of lepton-quark universality) the existence of a third family of quarks. In 1973 Kobayashi and Maskawa had already shown the need of a third quark family in order to incorporate CP violation in the Standard Model (S.M.).

The first fully reconstructed B mesons were reported in 1983 by the CLEO I collaboration. Since then the b-quark system has provided a great deal to our understanding of the S.M. The surprisingly long lifetime of the B mesons ($\sim$ 1.5 ps) provided the first evidence that the couplings given by the Cabibbo-Kobayashi-Maskawa (CKM) matrix (see Section A.1) could be different from 1 or λ ($\lambda \equiv \sin(\theta_{\text{Cabibbo}})$). The observation of mixing in the b-system by the ARGUS collaboration at DESY, again much larger than expected, was further evidence that this system can provide rich quantum mechanical phenomena.

Presently, one of the main goals of particle physics is to observe CP violation outside the Kaon system. The first observation of CP violation was reported about 30 years ago (see Appendix A) from the CPviolating decay $K_L^0 \to \pi^+\pi^-$, but so far there is not a clear understanding of its origins. The extremely successful S.M. predicts small CPviolating effects in the D system (mesons containing "charm") while substantial effects are expected in the B system [19, Chapter X].

Our present knowledge of the B system is primarily based on data obtained at e^+e^- colliders, in particular at machines operating at the $\Upsilon(4S)$ resonance. The irruption of hadron colliders as a viable alternative is a recent event. The first full reconstruction of B mesons at a hadronic machine was reported in 1992 by the CDF collaboration [4]. The observation was performed at PENN by Richard Hughes for his Ph.D. thesis. He measured a cross section of

$$\sigma(\bar{p}p \to bX; P_{Tb} \geq 11.5 \text{ GeV}/c, |y_b| \leq 1.0) = 6.1 \pm 1.9 \pm 2.4 \ \mu\text{b} \qquad (1.1)$$

using a sample of 14 events. The main advantage of a hadronic machine compared to an e^+e^- collider is a much higher cross section for producing b-quarks (50,000 nb compared to 1 nb for $\Upsilon(4S)$ machines). On the other hand, beauty is produced only in a tiny fraction of all collisions. Also, a typical b event has many more particles in a hadron machine than in an $\Upsilon(4S)$ e^+e^- collider. This led many to believe that B mesons could not be reconstructed cleanly enough to study CP violation in a hadron machine.

The measurement reported here demonstrates the possibility of very cleanly reconstructing the "golden mode" for the study of CP violation in a hadronic environment. The higher b-production rate of $\bar{p}p$ collisions results in our $J/\psi K^0_S$ sample of 36 events being larger than the 10 events sample reported by CLEO [3]. By the end of Run-Ia our sample was the largest in the world[1].

[1] New data taken during the ongoing Run-Ib makes the present $J/\psi K^0_S$ sample at CDF larger than the one reported here.

The study of CP violation is beyond the capabilities of the present experimental facilities [5]. The small branching ratio for the interesting modes (~ 0.0005 for the $J/\psi K^0_S$), and the need to identify the $B^0(\bar{B}^0)$ nature of the B-meson at production time, mean that huge numbers of b-quarks need to be produced. The alternatives so far are dedicated machines (the so called B-factories) or dedicated experiments at existing or future hadron machines. At the moment, two B-factories are being built (one at SLAC and one at KEK) while a fixed target experiment has been approved at DESY (HERA-B). There is also a proposal for a collider experiment (LHB) at the Large Hadron Collider at CERN (LHC).

1.2 Theoretical Context

The physics of hadrons containing beauty is expected to help in testing the present understanding of the Standard Model because the heavy mass of the b-quark allows for cleaner theoretical predictions than in other quark systems. From an experimental point of view, the long lifetime of the b-quark ($c\tau(B) \approx 0.045$ cm) and the first successful operation of a silicon vertex detector at a hadronic machine by the CDF collaboration has allowed significant progress in the isolation of b events.

The measurement the of ratio of branching ratios reported here can be shown to correspond to a measurement of the ratio of lifetimes $\tau(B^+)/\tau(B^0)$ by assuming the

following equality between the partial decay rates

$$\Gamma(B^+ \to J/\psi K^+) = \Gamma(B^0 \to J/\psi K^0) \tag{1.2}$$

The ratio of lifetimes is an important quantity to test the validity of the understanding of a heavy quark system. The naive spectator model assumes that the lifetime of a meson containing a heavy quark (c or b) is entirely determined from the properties of the heavy quark; that is, the light quark is a "spectator" in the decay (see left diagram in Fig. 1.1). This models predicts, in particular, a universal lifetime for all mesons containing the same heavy quark. In the charm quark sector this expectation is violated, the measured ratio of lifetimes being [48]:

$$\frac{\tau(D^+)}{\tau(D^0)} = 2.55 \pm 0.04 \tag{1.3}$$

The equality of the decay rates[2] can be motivated by realizing that the quark transition involved in the decays ($\bar{b} \to \bar{c}cs$) conserves isospin[3]; *i.e.* it commutes with the isospin operators. The initial and final states of both modes are isospin partners permitting us to write

$$\begin{aligned} < J/\psi K^+|\mathcal{O}(\bar{b} \to \bar{c}cs)|B^+ > &= < J/\psi K^0|\tau^-\mathcal{O}(\bar{b} \to \bar{c}cs)\tau^+|B^0 > \\ &= < J/\psi K^0|\mathcal{O}(\bar{b} \to \bar{c}cs)|B^0 > \end{aligned} \tag{1.4}$$

[2]A similar argument for D^+, D^0 semileptonic decay rates can be found in Ref. [19, Section IV.G].

[3]Isospin is an approximate symmetry of the strong interactions. In the quark model, the u and the d are in an isospin doublet. Isospin symmetry then means $m_u \approx m_d$. To a very good degree of approximation, the strong interaction does not distinguish a "down" quark from an "up" quark.

with τ^+, $\tau^- = (\tau^+)^\dagger$ the raising and lowering isospin operators. The same argument can be used for $\bar{b} \to \bar{c}l^+\nu$ and $\bar{c} \to \bar{s}l^-\bar{\nu}$[4].

Another way of motivating this assumption is by considering the main diagrams which contribute to both modes as shown in Fig. 1.1. In both diagrams the light quarks do not participate in the decay interaction, so no difference is expected. The non-spectator diagram shown in Fig. 1.2 —thought to play a role in the variations of lifetimes among B mesons—does not contribute to this decay as it requires the same quark flavour (q_α) in both final states.

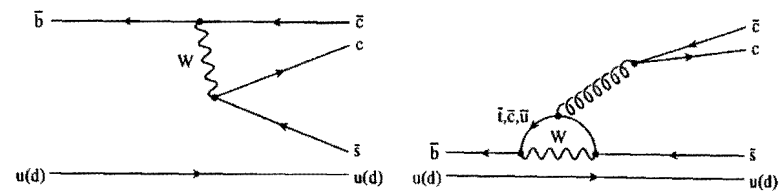

Figure 1.1: *Two diagrams [8] which contribute to the decay modes $B^+(B^0) \to J/\psi K^+(K^0)$. The left one is a spectator diagram, which is color-suppressed by the need to match the color of the decay products of the W with the color of the other quarks. The right one is a penguin diagram, which is suppressed because at least three gluons are needed to create the $J/\psi(\bar{c}c)$ state [9, Section 8.10]. The relative amplitude of the penguin diagram to the tree level diagram is expected to be $\sim 10^{-3}$ [21].*

[4]Thanks to Ikaros Bigi for pointing out this argument to us.

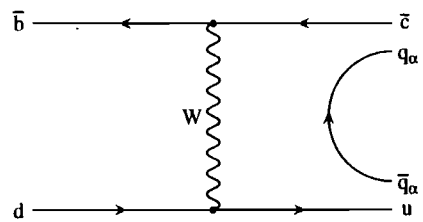

Figure 1.2: *Exchange diagram for B^0 decays. In this diagram the light quark participates in the interaction allowing differences between B^+ and B^0 decays. This diagram does not participate in the decay mode $B^0 \to J/\psi K^0$.*

With this assumption we then have:

$$\begin{aligned} \frac{BR(B^+ \to J/\psi K^+)}{BR(B^0 \to J/\psi K^0)} &= \frac{\Gamma(B^+ \to J/\psi K^+)/\Gamma(B^+ \to X)}{\Gamma(B^0 \to J/\psi K^0)/\Gamma(B^0 \to X)} \\ &= \frac{1/\Gamma(B^+ \to X)}{1/\Gamma(B^0 \to X)} \\ &= \tau(B^+)/\tau(B^0) \end{aligned} \tag{1.5}$$

A theoretical prediction based on QCD and using an expansion in $1/m_b$ is available in Ref. [2]. It gives

$$\frac{\tau(B^+)}{\tau(B^0)} \simeq 1 + 0.05\frac{f_B^2}{(200\ \mathrm{MeV})^2} \tag{1.6}$$

where f_B is the B meson decay constant which is estimated to be [7, Eq. (110)][19, Table 12] $f_B \approx 180 \pm 50$ MeV. This means that the ratio is expected to exceed 1.0

by a few percent to ten percent, in better agreement with the prediction of the naive spectator model. There is confidence that the ratio is greater than unity[5].

At the moment, CDF has a direct measurement of the individual lifetimes $\tau(B^+)$ and $\tau(B^0)$ [6] and obtains

$$\frac{\tau(B^+)}{\tau(B^0)} = 1.02 \pm 0.16\ (\mathrm{stat.}) \pm 0.06\ (\mathrm{sys.}) \tag{1.7}$$

The result presented in this thesis is complementary and independent of this measurement.

We expect that the methods developed for the ratio of branching ratios measurement can be directly applied to other decay modes already observed at CDF, for example $B^0 \to J/\psi K^{*0}$ and $B^+ \to J/\psi K^{*+}$ (see Section 5.5). This will have a twofold significance. By computing the ratio of branching ratios with respect to the $J/\psi K^{\pm}$ and then using the CLEO $BR(B^+ \to J/\psi K^+)$[6] we will be able to measure absolute branching ratios with better statistical significance than CLEO. Another use of the ratio of branching ratios is as a test of the applicability of the factorization hypothesis [10] for colour-suppressed processes [11]. We can readily see that the following relation holds:

$$\begin{aligned} R &\equiv \frac{BR(B^0 \to J/\psi K^{*0})}{BR(B^0 \to J/\psi K^0)} \\ &= \frac{\Gamma(B^0 \to J/\psi K^{*0})/\Gamma(B^0 \to X)}{\Gamma(B^0 \to J/\psi K^0)/\Gamma(B^0 \to X)} \end{aligned}$$

[5] Comment from Ikaros Bigi.

[6] This is CLEO's most populated B decay mode.

$$= \frac{\Gamma(B^0 \to J/\psi K^{*0})}{\Gamma(B^0 \to J/\psi K^0)} \tag{1.8}$$

with a similar relation for the charged modes. Models based on the factorization hypothesis can predict the ratio of decay rates R and the fraction of longitudinal polarization

$$\frac{\Gamma_L}{\Gamma} \equiv \frac{\Gamma(B \to J/\psi K^*)_L}{\Gamma(B \to J/\psi K^*)} \tag{1.9}$$

As shown in Ref. [12], the data available to date allow one to discard some models based on the factorization approach. There is a preliminary CDF result [13] for

$$\frac{\Gamma_L}{\Gamma} = 0.66 \pm 0.10^{+0.08}_{-0.10} \tag{1.10}$$

which could be complemented with a measurement of R.

Testing the applicability and limits of the factorization approach is important because it provides predictions for branching ratios for yet unobserved decay modes.

It is expected that CP violation should be manifested in the b-quark system. So far CP violation has only been observed in the Kaon system, but the theoretical implications remain uncertain [1, section 26.2.3][21]. The $B^0(\bar{B}^0) \to J/\psi K^0_S$ decay mode is considered to be the "golden mode" for the study of CP violation in the b-quark system because the theoretical implications of an observed asymmetry are very clean. We review a few concepts of CP violation in Appendix A and the theoretical simplifications that give the $J/\psi K^0_S$ the status it presently enjoys.

Chapter 2

THE COLLIDER DETECTOR AT FERMILAB

The CDF detector is a general purpose detector surrounding the B0 interaction region at the Fermilab Tevatron (see Section 2.1). It consists of a central and a forward/backward region where tracking, calorimetry, and muon detection subsystems are arranged to cover almost the entire solid angle. A perspective view is shown in Fig. 2.1. The components used for this analysis are all contained in the central region, where the combination of a 14.1 KG magnetic field and a large tracking chamber (CTC) permit a precise measurement of the momentum of charged particles. Two other tracking devices are present in this region: the SVX and the VTX, as shown in Fig. 2.2. Three sets of drift chambers are used to identify muons (CMU, CMP and CMX) by their penetration of the central calorimeter.

This section will first describe the accelerator and then the main components of the CDF detector which have relevance for this measurement. A more detailed overview of the detector can be found in Ref. [22].

Figure 2.2: *A cut-away view through the forward half of CDF. The detector is forward-backward symmetric. The emphasis is on the central detector, while the forward calorimeter is not to scale, but is included to illustrate the full CDF pseudorapidity range.*

2.1 The Tevatron at Fermilab

The Tevatron at Fermilab [23, 24, 38] is presently the most powerful accelerator in the world, providing $\bar{p}p$ collisions with a center of mass energy of 1.8 TeV. Its layout is shown in Fig. 2.3.

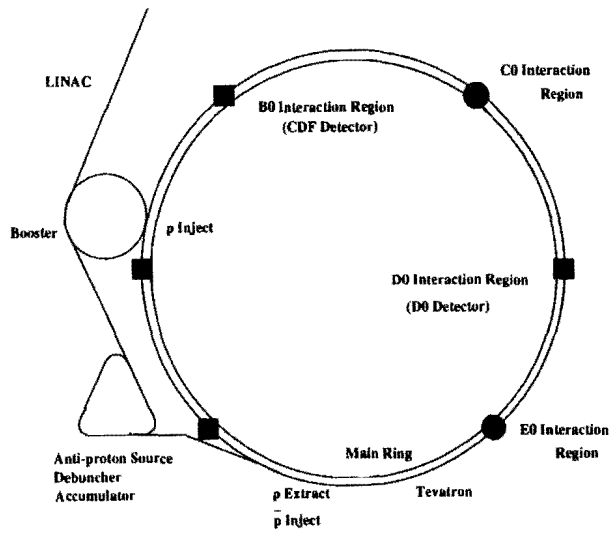

Figure 2.3: *Layout of the Fermilab Tevatron. It delivers collisions with a center of mass energy of 1.8 TeV. It is at present the world's most powerful accelerator*

The process of producing these collisions starts at a Cockcroft-Walton accelerator. This device adds an electron to hydrogen atoms and electrostatically accelerates the

H^- ions to 750 KeV. Then a linear accelerator 150 m long (the Linac) applies an oscillating electric field to increase the energy of the ions to 400 MeV. Before entering the third stage, the ions pass through a carbon foil which removes the two electrons. The third stage consists of a rapidly cycling synchrotron $\sim$ 150 m in diameter (the Booster) which increases the proton's energy to 8 GeV in approximately 20,000 revolutions. There are normally 12 bunches of proton's in the Booster, which are fed into the Main Ring, a synchrotron made out of 1,000 conventional, copper-coiled magnets. Presently the Main Ring increases the protons energy to 150 GeV. The final boost of energy is provided by the Tevatron, a synchrotron located directly below the Main Ring. Equipped with 1,000 superconducting magnets the Tevatron accelerates the protons to 900 GeV.

The antiprotons are produced by focusing 120 GeV protons from the Main Ring into a target. The collisions in the target produce a wide range of secondary particles including many antiprotons. These are selected and sent to the Debuncher where the momentum spread of the $\bar{p}$ sample is reduced by stochastic cooling. After this the antiprotons are moved to the Accumulator ring for storage. When enough antiprotons have been collected, they are injected into the Main Ring and then into the Tevatron where the energy is raised to 900 GeV.

2.2 The Central Tracking Chamber (CTC)

The CTC is the main tracking system at CDF, providing precise momentum measurements of charged tracks [25]. It is a large drift chamber with a length of 3.2 m and an external diameter of 276 cm. The chamber has 84 layers of sense wires arranged into 5 axial superlayers and 4 stereo superlayers. An axial superlayer contains 12 sense wires parallel to the symmetry axis. A stereo superlayer has 6 sense wires oriented at $\pm 3°$ (alternating between successive stereo superlayers) with respect to the symmetry axis and satisfying $r(z_M) = r(-z_M)$ where r is the distance to the origin in the x-y plane and z_M refers to the z-coordinate of the forward endplate. Within each superlayer, groups of sense-and field-wires are arranged in planes that configure cells inclined at an angle of 45° with respect to the radial direction (Fig. 2.4). This tilt is devised to compensate for the Lorentz angle[1], reducing dead time and linearizing the time-to-distance relationship at the end of the cells by making the drift trajectories approximately azimuthal. The large tilt angle results in an azimuthal overlap (about 20%), which guarantees that particles with $P_T > 2.5$ GeV/c will cross a plane of sense wires in each superlayer and generate a series of hits with small drift times. These "prompt" hits are used by the Central Fast Tracker (CFT) to reconstruct high momentum tracks on-line.

[1] In the presence of crossed magnetic and electric fields electrons drifting in a gas will approximately move at an angle β with respect to the electric field direction.

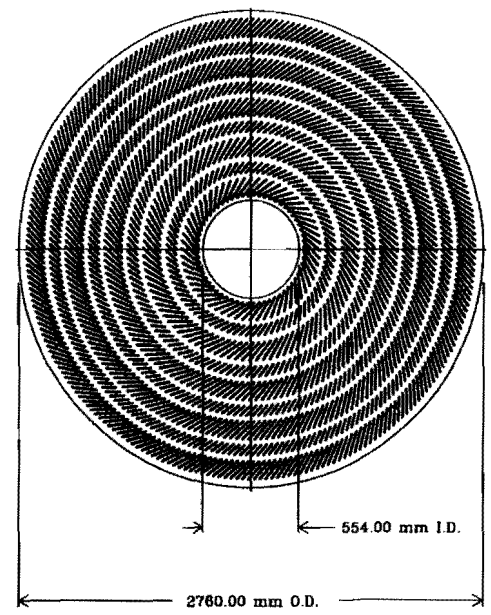

Figure 2.4: *End view of the Central Tracking Chamber showing the 9 superlayers and the azimuthal orientation of the cells.*

2.3 The Vertex Time Projection Chamber (VTX)

The VTX detector used for Run-Ia is an upgraded version of the similar detector used in the 88-89 run [26]. The VTX consists of 28 double time projection chambers (modules) located along the z-axis covering a length of 2.8 m and with a radius of 21 cm. The main purpose is to provide r-z information to complement the r-ϕ information provided by the CTC detector. It achieves a 2 mm z-vertex resolution for the primary vertex.

2.4 The Silicon Vertex Detector (SVX)

The SVX detector used for Run-Ia was the first silicon detector to be successfully operated in the environment of a hadron machine. With a measured impact parameter resolution for a single track of $\sigma = 13 + 40/P_T$ μm [27], this detector became a key element in the study of B-decays.

The Tevatron's $\bar{p}p$ collision point is distributed along the beamline with $\sigma = 30$ cm. This requires a long detector. The SVX detector consists of two barrels (an isometric view of one of them is shown in Fig. 2.5) each containing four radial layers of silicon strip detectors located between radiuses of 3.0 and 7.9 cm. Each layer is made out of twelve groups of silicon detectors. Each of these groups (a ladder) has three silicon detectors, 8.5 cm long, electrically bonded along z, so each individual readout channel sees a 25.5 cm long strip. A group of four ladders at a common azimuthal angle is

called a wedge. The silicon detectors are composed of p-type silicon strips deposited on an n-type silicon substrate 300 μm thick. The pitch of these strips is 60 μm for the three inner layers and 55 μm for the outermost layer. The charge deposited by an ionizing particle is detected by an IC located at the external end of the ladder. This chip amplifies, samples, sparsifies, and multiplexes data from 128 input channels which are DC coupled to the silicon strips. Given that the total number of SVX channels was 46080, sparsification of the data was necessary to reduce the size of the data read out.

Alignment

The SVX position relative to the CTC must be known precisely enough to render its measurements meaningful. Two procedures were used to determine the strip positions. During assembly the strips of the silicon detectors were measured directly with a TV camera to an accuracy of 2.5 μm. During installation of the VTX-SVX assembly into the CTC optical surveys were conducted. After installation, an off-line procedure using CTC tracks was used to align each barrel (treated as a rigid body) to the CTC, to align the individual ladders within a wedge, and to determine the wedge-to-wedge relative position.

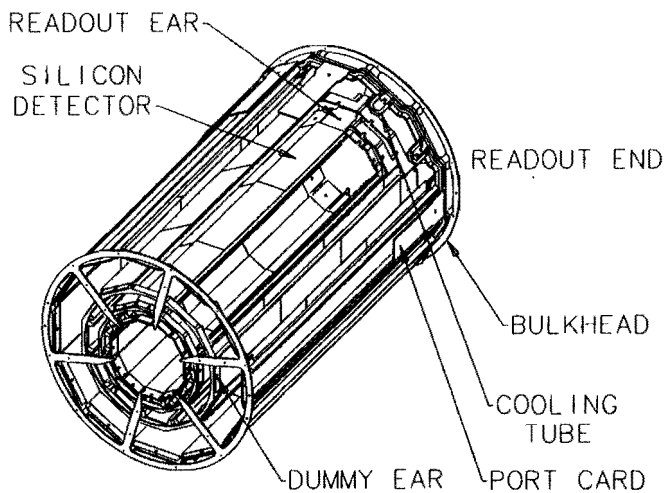

Figure 2.5: *An isometric view of one of the SVX barrels showing the four layers of ladders mounted on the beryllium bulkheads.*

The alignment of the three inner ladders implied radial shifts on all three layers which could be as large as 200 μm [27] for some of the ladders. The shifts are a systematic effect of unknown origin.

2.5 The Central Muon System (CMU)

The CMU consists of 48 groups of drift chambers located at the back of the hadron calorimeter (see Fig. 2.2 and Fig. 2.6). Each group is divided into 3 chambers (CMU modules), each chamber subtends $\sim 4.2°$ in azimuth. The location of the chambers within a central calorimeter wedge is shown in Fig. 2.6. The chambers (one is shown in Fig. 2.7) are composed of 16 cells arranged in four layers of 4 cells each. There are only 8 anode wires in a chamber because alternate cells in a layer share the same wire. The drift times at each layer (two are shown in Fig. 2.7) can be used to implement a Level 1 central muon trigger [28] by requiring

$$\mathrm{Min}(|t_4 - t_2|, |t_3 - t_1|) < t_{\mathrm{MAX}} \tag{2.1}$$

where t_{MAX} is a programmable threshold that can be varied in 1 ns steps. This requirement is equivalent to the condition of a maximum angle α between the muon candidate and the radial centerline (going through the origin of the CDF global coordinate system). Without considering multiple scattering, the angle α is related to the P_T of the muon, a larger α indicating a smaller P_T. Thus the Level 1 condition of a maximum drift time is equivalent to requiring a minimum P_T of the muon candidate.

Figure 2.7: *Cross section of a single muon chamber, showing drift times for layers 2 and 4. There are only 8 anode wires because alternate cells in a layer share the same wire.*

2.6 The Central Muon Upgrade (CMP)

This additional set of chambers is located behind steel shielding. The material in the calorimeters provides five absorption lenghts which added to the steel shielding results in a total of 8 absorption lengths. While reducing the punch-through contamination of the muon candidates, the extra shielding only allows for muons with $P_T > 2.5$ GeV/c to reach the CMP chambers. This reduces the importance of this system for our analysis. This system adds additional coverage beyond that of the CMU.

2.7 The Central Muon Extension (CMX)

This set of chambers provides additional coverage in the range $0.6 < |\eta| < 1$. During the early part of the run a very high rate of fake triggers was observed due to "fake" stubs. Many of these stubs originate from particles scattered off the beam pipe or the forward calorimeter by low angle tracks. To reduce this problem a new beam pipe with less material was installed mid-run to reduce the noise hits. For most of the run only muon candidates which passed the Level 2 trigger were considered in the J/ψ trigger. The hadronic energy deposited in the calorimeter tower associated with the muon candidate track was required to be greater than 0.5 GeV, as expected for a minimum ionizing particle from the interaction point.

Chapter 3

TRACKING AT CDF

An important difference between the modes under consideration comes from the characteristics of the final tracks. For the $J/\psi K^{\pm}$ mode the tracks identified as the $K^{\pm}$ are significantly harder than the tracks identified as π's from the $J/\psi K^0_S$ mode. Even more, the long lifetime of the K^0_S means that these tracks will have a large impact parameter with respect to the beam spot. The performance of the tracking algorithm for tracks with large impact parameter in a real event is expected to be worse than for tracks coming from the beam spot.

In this chapter we will describe the tracking algorithm used for Run-Ia.

3.1 CTC Tracking

The tracking algorithm used at CDF follows the usual prescription of splitting the task of track-finding into two stages [29, section 2.3]. The first stage is pattern recognition, where groups of hits in the detector are identified as belonging to a track. The second stage is fitting the hits to a track model. In the case of CDF, the track model is a

helix described by the 5 parameters $c, \phi_0, \cot\theta, d_0$ and z_0 (Appendix B).

3.1.1 General Scheme

The CTC tracking combines features from two independent algorithms, conventionally labeled "A" [30] and "B" [31]. The steering routine for pattern recognition and track fitting is **CTCDRV**. The steps followed by this routine are:

1. Do the pattern recognition in the r-ϕ plane. Use both algorithms "A" and "B" to identify tracks independently.
2. Delete extra versions of identical tracks.
3. Do the stereo pattern recognition and fit.
4. Apply selection criteria and delete tracks considered irrecoverable.
5. Attempt to recover tracks that failed but were not deleted by previous step. Also try to improve marginal successes.

Double versions of the same track are recognized by finding track pairs which share too many identical hits: only the "best" track is kept. The stereo pattern recognition procedure and the fit procedure from algorithm "A" are applied to all 2D tracks available at this stage. Only tracks that satisfy a set of quality requirements are kept. Tracks that fail the selection criteria are deleted except for those that have enough hits to likely be real tracks. The criteria used to keep a low-quality track is

- There are at least 16 hits in the inner 2 axial superlayers.
- There are at least 18 hits in the inner 3 axial superlayers.
- There are at least 27 hits.

About 95% of the kept low-quality tracks are stereo failures from algorithm "A". Approximately 25% of these can be saved by running the stereo pattern recognition from algorithm "B".

3.1.2 Tracking Algorithms

Here we describe the two tracking algorithms used for Run-Ia.

Algorithm "A"

- Find all line segments in the axial superlayers.
- Moving from the outermost to the innermost superlayer, find links between segments in the superlayer under consideration and unlinked segments in the two immediately outer axial superlayers or tracks already identified.
- Perform a fast approximate circle fit to all the axial hits associated with the track so far. This fit yields intermediate values for c, d_0 and ϕ_0.
- For each r-ϕ fitted track, hits on stereo cells which could have hits from the track under consideration are converted to a z position.

- A zero-gradient fitter is used to fit the 5 parameters simultaneously.

Algorithm "B"

- Find a "high quality" seed segment in an axial superlayer.
- Extend this seed segment in both directions. The initial step of this process uses the beam axis point to define an initial circular road where to look for hits. After a second segment has been found the beam position is not used.
- Perform a full axial fit.
- Do stereo pattern recognition for these fitted 2D tracks and perform a 5 parameter fit.

As expected [29, section 2.4.2] method "A" is the fastest and it is used for the Level 3 trigger.

The line segments for method "A" are found by looping over innermost wires, i. If wires i, $i+1$ and $i+2$ all have hits, loop over hits on wire i and $i+2$, ignoring hits marked as "noise" or as "used" by earlier tracking results. The hits from wires i and $i+2$ are used to provide a rough estimate of the aspect angle associated with each combination. Given that each wire may register several hits and each hit has an azimuthal ambiguity, there are several combinations which are sorted by increasing α; this means the algorithm searches for high-P_T tracks first. For each combination a

prediction for the drift time in layer $i+1$ is made and hits matching this prediction within a road are searched for on wire $i+1$. If an acceptable set of three hits is found then extra hits are searched for in the superlayer (neighbouring cells are included in the search). A search is considered a success if there are fewer misses than hits associated with the segment. A wire is considered a miss if no hit is found within the road and no preceding hit extends inside the road ("obscured" hit).

When a good line segment is found, the hit on wire i is marked as "used". The segment is also converted to an equivalent circle by assuming $d_0 = 0$ and taking the line as tangent to the circle. This allows us to compute c and ϕ_0 for all line segments.

To link segments across superlayers all equivalent circles in the outer superlayer are extrapolated to the center of the inner superlayer and an expected position, $\vec{r}_l'$, is computed. Then all inner segments are compared to these extrapolations, and a test is performed on the slopes of the segments.

The left drawing in Fig. 3.1 shows the two variables used to compare the extrapolated circle to the inner segment. The code requires $\epsilon < \pi/2$ and $l < 1$ cm. Because the extrapolation uses the assumption of $d_0 = 0$ these requirements are biased against large impact parameter tracks; for that reason the road is kept as wide as possible. The right drawing in Fig. 3.1 shows the angle-test applied to link candidates. Without resolution effects, the angles θ and θ' should match for segments tangential to the same circle. The code requires $|\sin(\theta - \theta')| < 0.025$.

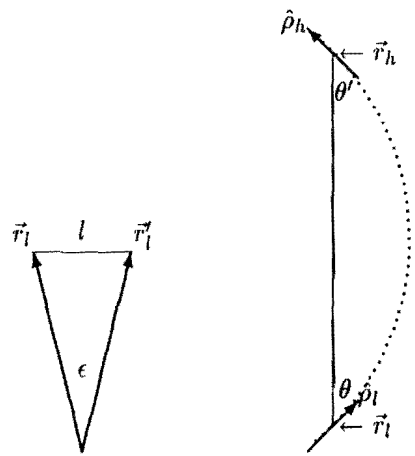

Figure 3.1: *Geometry for test used to link segments across superlayers. Left drawing shows variables used in the "position" test while right drawing shows angles θ and θ' used in the "angle" test [30].*

3.2 SVX Tracking

The SVX information is used to dramatically improve the impact parameter (d_0) and angle (ϕ_0) resolution of CTC tracks. It also improves the momentum resolution.

The SVX tracking algorithm uses the progressive method to associate hits in the SVX to tracks already found by the CTC. The algorithm starts with the CTC fit and then updates the track parameters whenever there is a new hit found in the SVX. The advantages of this procedure are [34]:

- The method is fast and stable.
- Pattern recognition and track fitting are done simultaneously. In case more than one candidate is found, the χ^2 is used to select the best candidate.
- Multiple scattering is treated correctly.
- Alignment corrections can be included each time a new hit is added.

The algorithm searches for hits around the intersection point of the extrapolated track and the measurement plane being considered; the track error matrix defines the size of the region where hits are searched for. When a track is extrapolated the effects of multiple scattering and ionization energy loss are accounted for. If a cluster is found the information is added to the fit and the procedure is repeated until all four SVX layers have been searched for hits. Track candidates are required to have at least two clusters in the SVX and a χ^2 below a certain value.

Chapter 4

DATA SAMPLE

The data used was collected during the 1992-1993 CDF run (Run-Ia) and corresponds to a total integrated luminosity of 19.3 pb^{-1}. At the Tevatron only one in about one thousand collisions produces a $b\bar{b}$ pair. Thus some selection mechanism is required that rejects minimum bias events and keeps b-events. The decay mode $J/\psi \rightarrow \mu^+\mu^-$ provides a simple trigger to select interesting events on-line. During Run-Ia a J/ψ sample was selected via a trigger set up in three levels of increasing complexity. A description of these levels follows.

4.1 J/ψ Trigger

The Level 1 central muon trigger requires a muon stub with $P_T > 2.0$ GeV/c.

The Level 2 central muon trigger requires that at least one of the Level 1 muons match a CFT track. The CFT only searches for tracks with $P_T > 3$ GeV/c, so requiring a CFT track imposes this higher P_T cutoff on one of the muons. There is also an extra requirement that the two Level 1 muons cannot be in adjacent modules

in ϕ if they are CMU. If one muon is CMX they cannot be in the same module. This separation requirement is needed to reduce backgrounds from punchthrough which are manifested as a cluster of muon stubs close to each other.

The Level 3 trigger uses a faster tracking algorithm than the one used offline to reconstruct tracks in the CTC. It also links muon stubs with CTC tracks. The matching between muon stubs and CTC tracks is required to be within 4σ. The $M(\mu^+\mu^-)$ of the surviving muon candidates is required to be within 600 MeV/c^2 of the J/ψ mass. Events passing all these requirements were written to tape for further processing offline.

4.2 Offline Production

At this level of the data-processing the detector information is analyzed and organized according to quantities of interest for physics analysis. Pattern recognition is run on the hit information collected by the CTC to form *track candidates*, and then a fit is performed to obtain track parameters from these candidates. Track segments from the muon chambers are linked with CTC tracks to form muon candidates.

4.3 J/ψ Candidate Events

To obtain the final sample of J/ψ candidate events we apply the following requirements on the matching quality between the stub in the muon system and the associated CTC

track:

- The $\chi^2_x < 9.0$. For μ's with hits in the CMU detector, χ^2_x is the one measured by that detector. If the muon has a CMP fit but not a CMU fit then χ^2_x is the one measured by the CMP system. If the muon only has a fit in the CMX system then we require $\chi^2_x < 12.0$.
- For CMU muons also require $\chi^2_x < 12.0$.

The $\mu^+\mu^-$ pairs satisfying all these requirements are then constrained to originate at a common vertex. The χ^2_F for this fit is required to satisfy $\mathrm{Prob}(\chi^2_F) > 0.01$. The resulting distribution of $M(\mu^+\mu^-)$ is shown in Fig. 4.1. The fitted function is the sum of two gaussians representing the J/ψ signal plus a constant term representing the background.

The final sample of J/ψ candidate events is obtained by simultaneously vertex and mass constraining the $\mu^+\mu^-$ pairs to the J/ψ mass and requiring that the increment in χ^2_F resulting from the mass constraint satisfy $\mathrm{Prob}(\Delta\chi^2_F) > 0.01$.

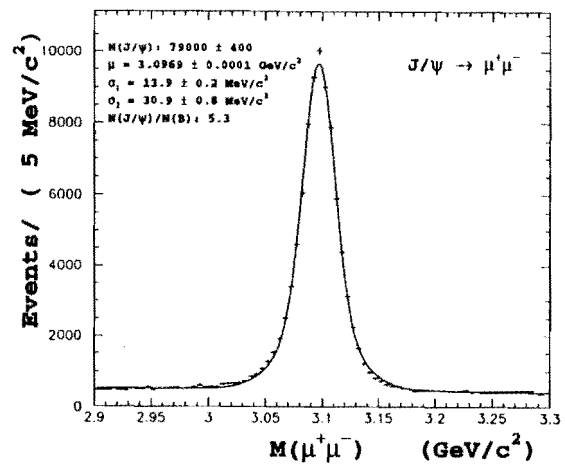

Figure 4.1: *Resulting distribution of $M(\mu^+\mu^-)$ for events satisfying requirements described in the text. Track parameters have been constrained to originate at a common vertex. The fitted function is the sum of two gaussians to represent the J/ψ signal plus a constant term to represent the background.*

Chapter 5

B MESON RECONSTRUCTION

In this chapter the selection criteria used to extract the different B signals are described and motivated. We also present the resulting distributions for three decay modes of interest to us.

5.1 Track Selection

The identification of exclusive decay modes of B mesons is accomplished via the distribution of the mass of the B candidates formed using the momenta of all daughters of the decaying B. It is important then to select tracks whose parameters are well measured. For tracks which only have CTC information, it turns out that it is enough to require the track information to be three dimensional. For tracks which have associated hits in the SVX the selection is more complicated due to random association of noise hits with the track. These noise hits will have two important effects. In general, these noise hits will steer the track parameters in random directions. Thus a track coming from the primary vertex will get steered away from the primary vertex and

may create fake secondary vertexes [35, section "Data selection"]. The second effect is that long lived particles like the K_S^0 or the Λ^0 will not point back to their point of origin, which will cause a decrease in efficiency when pointing constraints plus a quality of the fit cut are imposed on these particles.

5.1.1 SVX Track Selection for K_S^0 Reconstruction

We have made a study of the presence of spurious SVX hits on the tracks used to reconstruct the K_S^0 candidates [36]. To show the existence of bad SVX hits we select a sample of tracks which satisfy the following requirements:

- Both π tracks must have $d_\pi/\sigma_{d_\pi} > 3$. Here d_π is the π impact parameter with respect to the beam position and σ_{d_π} its uncertainty.
- The K_S^0 secondary vertex must be outside the active volume of the SVX.
- One of the tracks must have an SVX fit.

We show in Fig. 5.1 the normalized distribution of $M(\pi^+\pi^-)$. The existence of a K_S^0 peak proves the SVX hits are spurious. A selection algorithm is needed in order to reject bad SVX information for single tracks before they are used to search for K_S^0's.

There are two types of quantities which can be used to identify single tracks with bad SVX hits. One type is based on the χ^2_{SVX} from the fitted SVX clusters. The

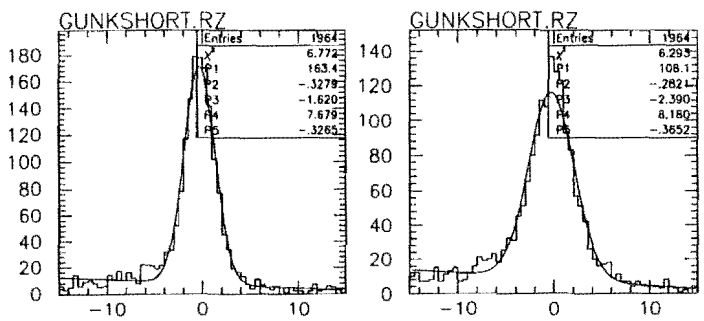

Figure 5.1: *Normalized mass distribution for K_S^0 candidates which decay outside the active volume of the SVX. One of the tracks is required to have an SVX fit thus demonstrating the presence of spurious hits. Left plot shows the resulting distribution when only the CTC information is used for both tracks. Right plot shows the effect of using the bad SVX information. There is a considerable widening of the distribution from $\sigma = 1.6$ to $\sigma = 2.4$.*

other one is based on requiring high quality SVX clusters. For our study we defined a high quality cluster to be:

- The cluster is not shared with other tracks.
- The cluster has no dead strips.
- The length of the cluster is less than 4 strips.

We considered three SVX selection algorithms and rated them according to the number of K_S^0's found by the following K_S^0 finder scheme:

- The SVX information for an individual track is used only if it passes the SVX selection algorithm under consideration.
- The SVX information is rejected if the $\pi^+\pi^-$ has only one track with SVX hits or if the decay vertex is outside the third SVX layer.
- $d_\pi/\sigma_{d_\pi} > 3$ and $d_K/\sigma_{d_K} < 5.0$. Here d_K is the K_S^0 impact parameter with respect to the primary vertex and σ_{d_K} its uncertainty.

The three SVX selections are labeled "A", "B" and "C" and are defined as follows:

"A" Require $\delta\chi^2 < 6$, with $\delta\chi^2$ defined to be the increment of the $\chi^2_{\rm SVX}$ when a cluster is added to the fit. Also require one of the clusters to be a high quality cluster.

"B" When fitting the track to the clusters only consider clusters for which $\delta\chi^2 < 6$. Also require one of the clusters to be a high quality cluster.

"C" Require $\chi^2_{SVX}/\text{nhits} < 6$ and at least two high quality clusters [37].

In Table 5.1 we show the performance of each selection algorithm. For comparison the entry "CTC only" shows results when the SVX information is not used. The column labeled "% increase" shows the % of extra K^0_S's that we find by using the SVX information. The column "% SVX-SVX" shows the percentage of $\pi^+\pi^-$ combinations which have an SVX fit. The "S/N" column shows the S/N ratio from the K^0_S mass peak.

We conclude that:

- Algorithm "C" gives us the highest number of K^0_S's.
- Between 20 and 30 % of the reconstructed K^0_S's have SVX information which passes our quality requirements.
- The proper use of the SVX information increases the K^0_S reconstruction efficiency by about 20% but it does not improve the S/N ratio of the K^0_S.

Finally, we choose the following SVX selection algorithm when reconstructing K^0_S's.

The SVX information is used only if:

Table 5.1: *The effect of different SVX track selection algorithms. Left numbers are for runs earlier than 42000 while right ones are for runs later than 46000.*

Algorithm	# K^0_S	% increase	S/N	% SVX-SVX
CTC only	2810/6012	0/0	13/15	0/0
"A"	3300/6730	17/12	14/14	23/18
"B"	3400/6870	21/14	12/12	29/24
"C"	3450/6970	23/16	14/14	28/21

- The $\chi^2_{SVX}/\text{nhits} < 6$ where nhits is the number of fitted SVX clusters.
- If nhits = 4 the SVX fit is accepted. For nhits = 2, 3 we further require at least two high quality clusters.
- Both tracks must have SVX information and the reconstructed 2-D vertex must be inside the area defined by the third SVX layer.

If these requirements are not met the CTC information is used instead.

5.1.2 SVX Track Selection for Other Tracks

By reconstructing several B decay modes (we have looked at $B^0 \to J/\psi K^*(892)^0$ in addition to the modes shown later in this chapter) we realized that the $M(B)$ resolution improves slightly when a more relaxed set of SVX requirements is applied

to the other tracks used for the $M(B)$ reconstruction.

For tracks that are not used to reconstruct a K_S^0 candidate the SVX information is used only if:

- The $\chi^2_{SVX}/\text{nhits} < 6$ where nhits is the number of fitted SVX clusters.
- If nhits $= 3, 4$ the SVX fit is accepted. For nhits $= 2$ we further require at least one high quality cluster.

If these requirements are not met the CTC information is used instead.

5.2 Improving the Tracking Resolution

The track reconstruction algorithm described in Chapter 3 is intended to reconstruct tracks without making use of the information provided by the assumed track production mechanism. For instance, the $\mu^+\mu^-$ track candidates used to reconstruct the J/ψ should originate from a common vertex.

When searching for a specific physical process, the extra information available can be used to improve the track parameters by imposing extra conditions. The use of constraints is also useful to eliminate background by first imposing the given constraint and then cutting on the "quality of the fit" χ^2_F. By increasing the number of constraints applied it is possible to define an incremental χ^2_F which is the increment in χ^2_F when new constraints are imposed.

For Run-Ia a software package was available that allowed us to impose the following requirements:

- A set of tracks could be forced to originate from a common vertex. This is called a vertex constraint.
- The line along the total momentum of tracks originating at a common vertex could be forced to include a given point. This is called a point constraint. This constraint could be imposed in the x-y plane only (called a 2D point constraint) or in three dimensions (called a 3D point constraint).
- The mass of a set of tracks could be forced to some value. This is called a mass constraint.

The code allowed for several secondary vertexes and one primary vertex.

5.2.1 Constraints for the $J/\psi K^\pm$ Mode

The following is an ordered list of the constraints applied to the tracks used to reconstruct this mode.

- The $\mu^+\mu^-$ tracks should originate at a common vertex.
- The $M(\mu^+\mu^-) = M(J/\psi)$.
- The $\mu^+\mu^-$ tracks plus the $K^\pm$ track candidate should originate at a common vertex.

- A 2D and then a 3D point constraint to the primary vertex is imposed on the $\mu^+\mu^- K^\pm$ system.

5.2.2 Constraints for the $J/\psi K_S^0$ Mode

The following is an ordered list of the constraints applied to the tracks used to reconstruct this mode.

- The $\mu^+\mu^-$ tracks should originate at a common vertex.
- The $M(\mu^+\mu^-) = M(J/\psi)$.
- The $\pi^+\pi^-$ track candidates should originate at a common vertex.
- The $M(\pi^+\pi^-) = M(K_S^0)$.
- A 3D point constraint to the $\mu^+\mu^-$ vertex is imposed on the $\pi^+\pi^-$ total momentum.
- A 2D and then a 3D point constraint to the primary vertex is imposed on the $\mu^+\mu^- K_S^0$ system.

5.3 Kaon Selection

During the 1992-1993 run, CDF did not have a particle ID system which could differentiate Kaons from pions in the P_T range of interest (roughly $P_T > 0.5$ GeV/c for B events passing the J/ψ trigger). To select the $K^\pm$ track candidates we use the

fact that particles from B decays have a P_T distribution which is harder than the background around the B mass [38, Fig. 7.4].

The $c\tau(K_S^0) = 2.676$ cm allows one to reconstruct a very clean K_S^0 signal by applying cuts on d_π/σ_{d_π} and the $L_{xy}(K_S^0)$. In Fig. 5.2 we show the K_S^0 sample used in the B^0 reconstruction. We have required $d_\pi/\sigma_{d_\pi} > 2$, $L_{xy}(K_S^0) > 1.0$ cm and $\mathrm{Prob}(\Delta\chi^2_F) > 0.01$ for the vertex and point constraint increments of χ^2_F. Here $L_{xy}(K_S^0)$ refers to the K_S^0 decay length with respect to the beam position along the K_S^0 momentum. If we define $\vec{x}_S$ to be the K_S^0 decay point, $\vec{x}_P$ the beam position, and $\hat{P}$ the direction of the momentum of the K_S^0 we then have

$$L_{xy}(K_S^0) = (\vec{x}_S - \vec{x}_P) \cdot \hat{P} \tag{5.1}$$

where all vector quantities are in the x-y plane.

Having a clean Kaon signal for the $J/\psi K_S^0$ mode but not for the $J/\psi K^\pm$ mode results in very different signal-to-noise ratios for the reconstructed B signals. This indicates that Kaon ID is an important component for a detector trying to do B physics in a hadron collider.

5.4 Combinatoric Background Reduction

The J/ψ sample defined in Chapter 4 has been shown to have a "prompt" component with no lifetime and a long lived component which is supposed to originate from $B \to J/\psi X$ [40, Page 1]. We show these two components in Fig. 5.3. The quantity

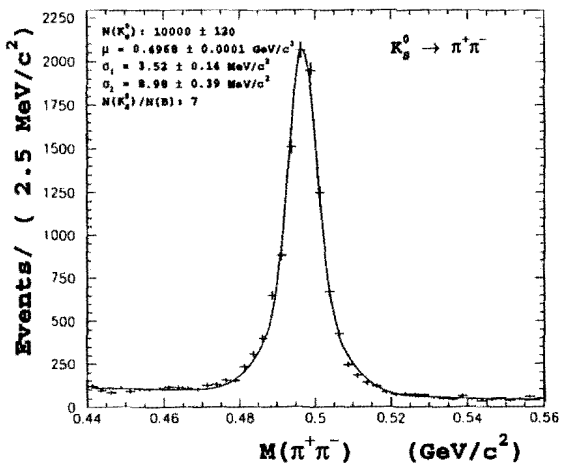

Figure 5.2: *Distribution of $M(\pi^+\pi^-)$ for K_S^0 candidates used in the B^0 reconstruction. The K_S^0 signal is very clean and allows for a significant reduction of the combinatorial background around the B^0 signal.*

plotted is λ which is defined to be the "pseudo"-$c\tau(B)$ computed with $\mu^+\mu^-$ measured quantities plus a correction factor to take into account the missing P_T carried by X. It is possible to obtain the fraction of J/ψ's which come from a B by fitting the λ distribution to a prompt component (to model the J/ψ's with no lifetime) plus a long lived component (for the J/ψ's from B's) plus an extra function obtained from the J/ψ sidebands [41] (to model the continuum under the J/ψ). For J/ψ's with $P_T > 4$ GeV/c the B fraction is found to be $19.6 \pm 0.4\%$. The data can be split in P_T bins and a B fraction is obtained for each bin. This way the B fraction is shown to increase smoothly from $13.3 \pm 0.5\%$ for $4 < P_T < 5$ GeV/c, to $42.1 \pm 4.9\%$ for $13 < P_T < 14$ GeV/c.

The 20% B purity of the J/ψ sample added to the presence of extra tracks in B events produced by the hadronization of the b-quark and the underlying event require the use of selection cuts to reduce the combinatorial background to the B signal. Hadronization refers to the process by which a parton from a high energy collision acquires a partner from the vacuum to form a colourless meson or baryon. This process induces other tracks around the original parton. The underlying event refers to the tracks created by the fragments from the $\overline{p}p$ collision.

For Run-Ia data there were four types of selection criteria successfully used to extract different B signals. These criteria are summarized below:

1. P_T cuts on the extra tracks used to form the $M(B)$.

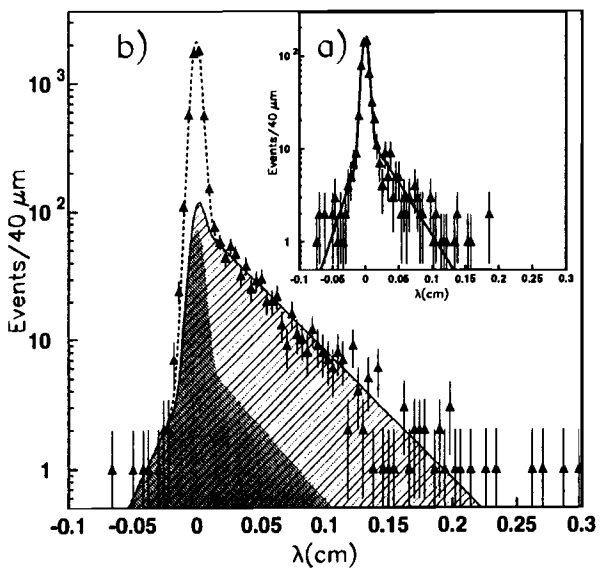

Figure 5.3: *Distribution of λ (pseudo-$c\tau$) for the J/ψ sample with both muons in the SVX [40]. Inset shows the λ distribution for the J/ψ sidebands while main plot shows the distribution for the J/ψ signal regions.*

2. Cuts requiring a B vertex that is displaced from the primary vertex.

3. Cuts requiring that the topology of the tracks used to form the $M(B)$ be consistent with the specific decay mode.

4. Isolation cuts using the empirical observation that the fraction of P_T carried by tracks around the B candidate is smaller for B events than for the background events [42].

The combination of criteria 2 and 3 provides a very powerful rejection of the combinatorial background by first incrementing the B purity of the J/ψ sample and then rejecting tracks which are not consistent with coming from the secondary vertex determined by the $\mu^+\mu^-$ pair. At a hadron machine an important contribution to the combinatorial background comes from tracks originating at the primary vertex.

For the B signals reconstructed in this thesis we have only used cuts based on criteria 1 through 3.

5.5 $B^\pm \to J/\psi K^{*\pm}$ Decay Mode

As an independent example of the B reconstruction methods we show the mode $B^\pm \to J/\psi K^{*\pm}$ which we observed for the first time at CDF. The $K^{*\pm}$ is reconstructed via the decay chain $K^{*\pm} \to K^0_S \pi^\pm$. The cuts applied are:

- Both muons have SVX information.

- $c\tau(B) > 0.01$ cm.
- $P_T(B) > 6$ GeV/c, $P_T(K^{*\pm}) > 1$ GeV/c, $P_T(\pi^{\pm}) > 0.5$ GeV/c.
- $d_\pi/\sigma_{d_\pi} > 2$, $L_{xy}(K_S^0) > 0$.
- $|M(K_S^0\pi^{\pm}) - M(K^{*\pm})| < 0.08$ GeV/c^2.
- $\mathrm{Prob}(\Delta\chi_F^2) > 0.01$.

We show the resulting distribution in Fig. 5.4. The signal is very clean due to the clean K_S^0 sample shown earlier (Fig. 5.2) and the requirement of SVX information on the muon tracks.

5.6 $B^{\pm} \to J/\psi K^{\pm}$ and $B^0(\bar{B}^0) \to J/\psi K_S^0$ Modes

To isolate the B signals used in this measurement we require the following set of cuts.

Cuts common to both modes

- One μ must have $P_T > 1.8$ GeV/c and the other one $P_T > 2.5$ GeV/c.
- The $\mu^+\mu^-$ must satisfy the trigger requirements.
- $c\tau(B) > 0.01$ cm.
- $P_T(B) > 7$ GeV/c, $P_T(K) > 1.5$ GeV/c.

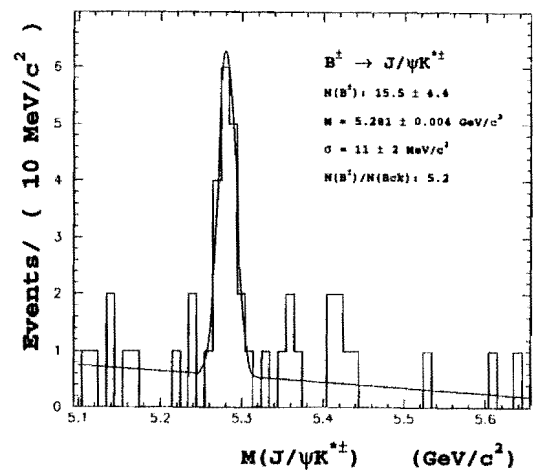

Figure 5.4: *Mass distribution for $J/\psi K^{*\pm}$ decay mode. The selection requirements are described in the text. Both muons have been required to have SVX information*

- Prob($\Delta\chi^2_F$) > 0.01 where $\Delta\chi^2_F$ is the increment in χ^2_F after a new constraint has been added.

- The $K^\pm$ track and π's tracks must satisfy $R_E > 86$ cm.

Here R_E refers to the radius at which a given track leaves the volume of the CTC. The relations used to compute R_E are described in Appendix B.

Extra cuts for $J/\psi K^0_S$ mode

- $d_\pi/\sigma_{d_\pi} > 2$ with d_π the π track impact parameter with respect to the beam position.

- The $L_{xy}(K^0_S) > 1$ cm.

- $P_T(\pi) > 0.35$ GeV/c.

The $c\tau(B)$ is computed with the J/ψ secondary vertex and the $P_T(B)$. This way we eliminate the systematic effect coming from the different number of SVX tracks the two modes have. The trigger and P_T requirements on the muon tracks are needed to allow for a good M.C. simulation of the Kaon spectrum. The $R_E > 86$ cm and $P_T(\pi) > 0.35$ GeV/c cuts are required to use our measured value of the tracking efficiency.

The resulting mass distributions are shown in Fig. 5.5 and Fig. 5.6.

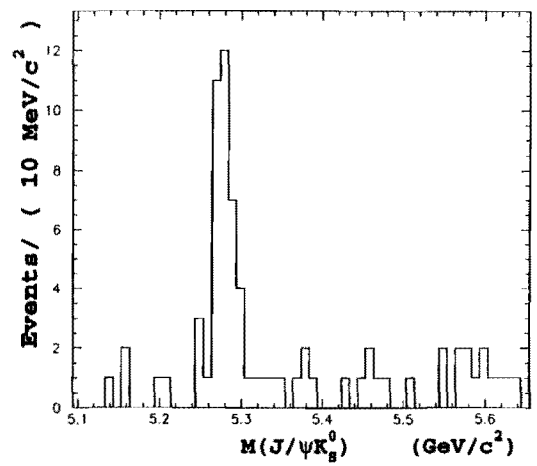

Figure 5.5: *Mass distribution for $J/\psi K^0_S$ decay mode plotted in 10 MeV/c^2 bins.*

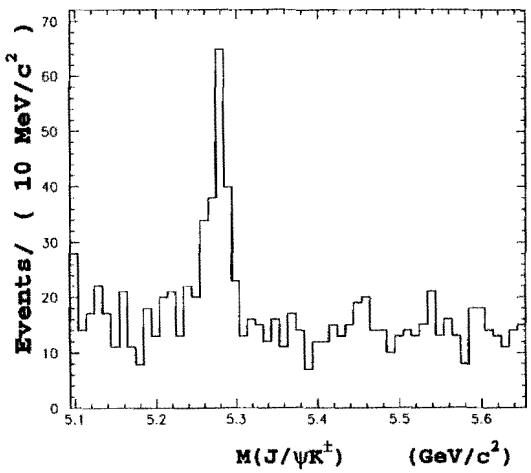

Figure 5.6: *Mass distribution for $J/\psi K^{\pm}$ decay mode plotted in 10 MeV/c^2 bins.*

Chapter 6

MEASURING THE RATIO OF BRANCHING RATIOS

In this chapter we discuss the relationships and quantities needed to determine the ratio of branching ratios.

6.1 Method

The basic relations between the observed number of events and the branching ratios for each mode are shown in Eq. 6.1 and Eq. 6.2.

$$\mathcal{L} \times \sigma(\bar{p}p \to \bar{b} \to B^+) \times BR(B^+ \to J/\psi K^+) \times \epsilon_{B^+} = N(J/\psi K^+) \tag{6.1}$$

$$\mathcal{L} \times \sigma(\bar{p}p \to \bar{b} \to B^0) \times BR(B^0 \to J/\psi K^0) \times \epsilon_{B^0} = N(J/\psi K^0_S) \tag{6.2}$$

Here $\mathcal{L}$ is the integrated luminosity, ϵ_{B^+} and ϵ_{B^0} are the reconstruction efficiencies for each mode including the branching ratios $BR(J/\psi \to \mu^+\mu^-)$ and $BR(K^0_S \to \pi^+\pi^-)$.

At this point we need to assume that the probability of the process $\bar{b} \to B^+$ is the same as for the process $\bar{b} \to B^0$. This assumption has been used before at CDF (see

Ref. [38] and references therein). A $b\bar{b}$ quark pair will fragment in an isospin-invariant manner as long as it does not interact with the fragments from the $\bar{p}p$ collision [39]. This is expected to hold in the central region at high momentum transfers.

We then obtain the following expression for the ratio of branching ratios

$$\frac{BR(B^+ \to J/\psi K^+)}{BR(B^0 \to J/\psi K^0)} = \frac{N(J/\psi K^\pm)}{2N(J/\psi K^0_S)} \times \frac{\epsilon_{B^0}}{\epsilon_{B^+}} \tag{6.3}$$

where the factor of 2 is a consequence of the fact that the K^0 decays as a K^0_S only 50% of the time; when it decays as a K_L we lose the event because CDF cannot detect K_L's.

6.2 Determining the Number of Observed Events

We determine the number of observed events for each mode from Fig. 6.1 and Fig. 6.2. These plots show the distribution of normalized mass, *i.e.*, we compute the mass of the B candidate, subtract the B mass and divide by the uncertainty of the mass measurement computed using the errors on the track parameters. We use the normalized mass because we are mixing data that have tracks in the SVX with data that only have CTC tracks. These two sets of data have different mass resolutions. Dividing by the predicted resolution takes care of this effect.

A binned-maximum-likelihood method [38, Section 7.5] is used to fit the number of observed events. The function fitted is

$$f(m) = N_S \times \mathrm{bw}\frac{1}{\sqrt{2\pi}\sigma}\exp(-\frac{(m-\mu)^2}{2\sigma^2}) + N_B \times \frac{\mathrm{bw}}{5\sigma} \tag{6.4}$$

where bw is the bin width.

The fit is performed with the software package PAW. This code evaluates the function f at the center of each bin to obtain a prediction for the number of entries per bin. It then varies N_S, μ and N_B to maximize the log-likelihood function (we fix $\sigma = 1.0$).

To compute the number of entries predicted by the function f we simply sum across the bins of interest

$$N = \sum_i f(m_i) \approx \int \frac{f(m)}{\mathrm{bw}} dm \tag{6.5}$$

The number of signal events is then given by N_S and the number of background events in a $\pm 2.5\sigma$ region around the fitted mean μ is given by N_B.

In Table 6.1 we summarize the number of fitted events for each decay mode.

Table 6.1: *Number of fitted events (N_S) from distributions shown in Fig. 6.1 and Fig. 6.2.*

Decay Mode	N_S
$J/\psi K^0_S$	36.0 ± 6.4
$J/\psi K^\pm$	139.3 ± 15.7

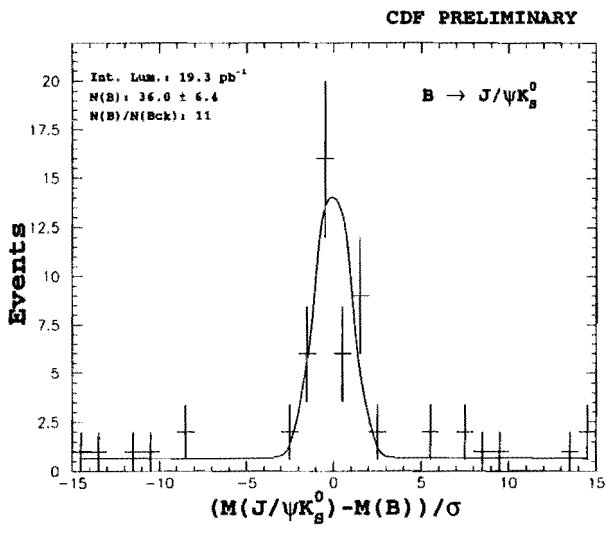

Figure 6.1: *Normalized mass distribution for $J/\psi K^0_S$ decay mode plotted in bins of width 1.*

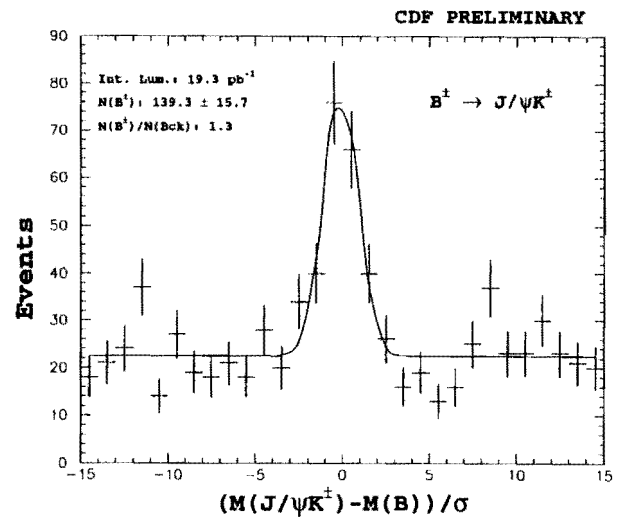

Figure 6.2: *Normalized mass distribution for $J/\psi K^\pm$ decay mode plotted in bins of width 1.*

Chapter 7

CTC TRACKING EFFICIENCY

The description of the details of the tracking algorithm "A" indicates that the performance of the algorithm may be lower for soft tracks, large impact parameter tracks, and tracks in "busy" environments. The pion tracks from the K_S^0 will be softer and have larger impact parameters than the $K^\pm$ tracks, so a different efficiency may be expected for the two B decay modes. In this chapter we report on the measurement of the tracking efficiency used in this analysis.

To measure the tracking efficiency we embed M.C. tracks in data J/ψ events. We developed a new technique which orients the M.C. tracks with respect to the J/ψ from the data in a way which permits the reconstruction of the B mass after the whole event has been retracked. This allows a more realistic definition of the tracking efficiency than the definitions used by previous analyses. We have also allowed the $K^\pm$ tracks to decay, which is an improvement over all previous treatments [32].

We provide a summary of the procedure. A detailed report can be found in

Ref. [33].

7.1 Method

The algorithm used is detailed here.

1. For each J/ψ event, several M.C. events are generated for the particular decay mode under consideration.
2. The tracks related to the Kaon (the Kaon itself for the $K^\pm$ and the pions for the K_S^0) are rotated to keep their relative orientation to the J/ψ direction. The rotated tracks are required to be within the geometrical acceptance of the detector.
3. A simulation program is used to generate the hits these tracks would produce in the CTC. The same program is used to merge these hits into the data event.
4. The event is retracked.
5. The embedded tracks are searched for.

To rotate the momenta we used the formula described in Appendix C. This is a new procedure which allows us to reconstruct the B mass after retracking the event. The definition of the tracking efficiency is then straightforward using the fitted number of B's from the mass distribution of all B candidates in the event. To form the B candidates we use all the tracks in the event.

The procedure of making a 3D rotation on the final tracks does not conserve the P_T of the rotated tracks. The tracking efficiency is a function of the P_T so this effect could skew our results. We checked that, on average, the P_T distributions before and after the rotation are the same.

A track generated with the M.C. may not be reconstructed because it does not go through the active volume of the CTC or because of inefficiencies of the tracking algorithm. To disentangle the inefficiency coming from the geometrical coverage of the detector from the inefficiency coming from the tracking algorithm we compute the "exit radius" (from now on R_E) of the helix as explained in Appendix B.4 and measure the tracking efficiency only for tracks with $R_E > 86.0$ cm

The routine used to generate the hits receives as input the helix parameters for the particular track and starting and ending radiuses between which the simulation takes place. It then applies dE/dx losses and multiple scattering smearing to simulate the effect of the material from the starting radius of the particle to the inside of the CTC. This means that particles from secondary vertices, like the $\pi^+\pi^-$ from the K_S^0 vertex, are scattered less than particles from the primary vertex.

7.2 Efficiency Definition

There are two definitions available for the tracking efficiency measurement. The knowledge of the original track parameters of the embedded track allows one to search

for it in the reconstructed event by comparing the original parameters to the parameters of all tracks in the event. This definition has the following characteristics:

- It allows one to measure a "single" track efficiency, as it is possible to identify an embedded track as "found" or "lost".
- It is not realistic when compared to the B reconstruction procedure followed in the data for which we never have the original track parameters.

To implement this definition we define a "matching χ^2" as

$$\chi^2_M = \Delta h^T \, \mathrm{Cov}^{-1}(h) \, \Delta h \tag{7.1}$$

where Δh refers to the difference between the reconstructed track parameters and the original track parameters and $\mathrm{Cov}(h)$ is the covariance matrix for the reconstructed track (with parameters h). We define a track to be "found" by the χ^2_M method if there is at least one track in the retracked event with $\chi^2_M < \alpha$ where α depends on the starting radius of the particle [33].

We can provide a more realistic measurement of the efficiency than the χ^2_M definition because our embedding algorithm allows us to reconstruct a B peak after retracking. We define the tracking efficiency to be the ratio of fitted B events in the peak to the number of embedded Kaons. This definition has the following characteristics:

- There is no way of knowing whether a particular track has been found or not. We are only concerned with the total number of reconstructed B's.
- It is more realistic than the previous definition as it follows the usual B reconstruction procedure more closely.

7.3 Tracking Efficiency Results for $J/\psi K^{\pm}$ Mode

To estimate the importance of modeling the finite lifetime of the $K^{\pm}$ we show results for the case when the $K^{\pm}$'s are not allowed to decay (all previous measurements have imposed this restriction). In Fig. 7.1 we show the tracking efficiency as a function of $P_T(K^{\pm})$ together with the reconstructed B peak after retracking the event. The P_T curve quickly reaches a plateau, so we fit a constant value for $P_T > 1$ GeV/c. The fit gives an efficiency of $97.4 \pm 0.1\%$. The mass plot is for embedded tracks with $P_T > 1$ GeV/c. By fitting the number of reconstructed B events and taking the ratio to the number of embedded Kaons we get an efficiency of $96.5 \pm 0.7\%$. The small difference between these two methods is taken as a systematic error. We estimate a 1% upper bound for this uncertainty.

We now proceed with the full simulation. The $K^{\pm}$'s are allowed to decay according to Table 7.1. The charged daughters from the decay are also embedded.

In Fig. 7.2 we show the tracking efficiency as a function of $P_T(K^{\pm})$ together with the reconstructed B peak after retracking the event. The P_T curve slowly reaches a

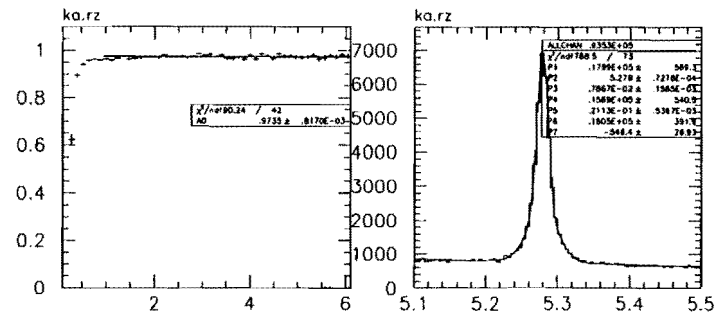

Figure 7.1: *Tracking efficiency for embedded $K^{\pm}$ tracks. The $K^{\pm}$'s are not allowed to decay. Left plot shows the tracking efficiency (according to the χ^2_M definition) as a function of P_T. Right plot shows the reconstructed B peak after retracking the event.*

plateau. We fit a constant value for $P_T > 3$ GeV/c. The fit gives an efficiency of $94.6 \pm 0.2\%$. The mass plot is for embedded tracks with $P_T > 1$ GeV/c. The efficiency from the mass plot is measured to be $91.0 \pm 0.6\%$.

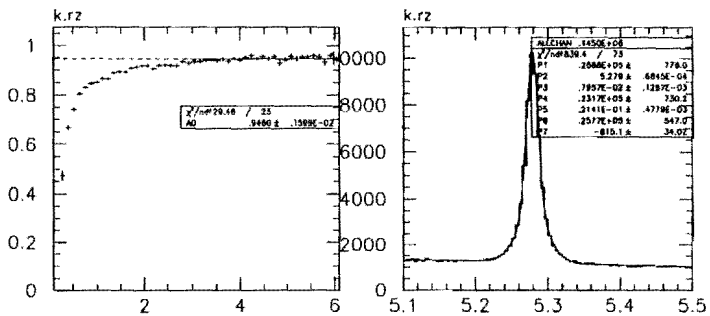

Figure 7.2: *Tracking efficiency for embedded $K^{\pm}$ tracks. The $K^{\pm}$'s are allowed to decay. Left plot shows the tracking efficiency (according to the χ^2_M definition) as a function of P_T. Right plot shows the reconstructed B peak after retracking the event.*

We conclude that, as expected, the finite lifetime of the $K^{\pm}$ lowers the tracking efficiency ($\sim 6\%$ for $P_T(K^{\pm}) > 1$ GeV/c). Softer tracks have a higher chance to decay before crossing enough CTC wires, thus the loss in tracking efficiency is greater for softer tracks.

7.3.1 Systematic Effects for the $J/\psi K^{\pm}$ Mode

We study the effect of the topology of the data events used. The event topology for events with a J/ψ produced in the decay of a B meson will differ from a generic J/ψ event. Given that the tracking efficiency depends on the number of tracks nearby, we need to check how much our result depends on the event topology. We estimate the importance of this effect by requiring the di-muon pair to have an SVX fit. We then measure the efficiency with and without a $c\tau$ cut on the J/ψ vertex. The $c\tau$ cut greatly increases the B purity of the sample allowing us to estimate the size of the systematic introduced by the event topology.

We measure the tracking efficiency to be $91.1 \pm 0.9\%$ when no $c\tau$ cut is applied and $91.1 \pm 1.6\%$ when a $c\tau > 0.01$ cm is applied. We conclude that the event topology of the J/ψ events does not contribute a significant systematic error to our measurement.

We also measure the probability that a track found by one efficiency definition fails when the other definition is used. About 1% of the tracks show this behaviour.

Finally we assign a 1.4% systematic error to the measurement of the tracking efficiency.

7.3.2 Tracking Efficiency for the $J/\psi K^{\pm}$ Mode

We have measured the tracking efficiency for $P_T(K^{\pm}) > 1.0$ GeV/c to be 91.0 ± 0.6 (stat.) ± 1.4 (sys.)%.

Table 7.1: *List of simulated decays for the $K^{\pm}$.*

K^+ Decay Modes	Fraction (Γ_i/Γ)
$\mu^+\nu_\mu$	63.5 %
$\pi^+\pi^0$	21.2 %
$\pi^+\pi^+\pi^-$	5.6 %
$\pi^+\pi^0\pi^0$	1.7 %
$\mu^+\nu_\mu\pi^0$	3.2 %
$e^+\nu_e\pi^0$	4.8 %

7.4 Tracking Efficiency Results for the $J/\psi K_S^0$ Mode

In Fig. 7.3 we show the dependence of the tracking efficiency as a function of d_0 (the track impact parameter). As expected the efficiency lowers with d_0.

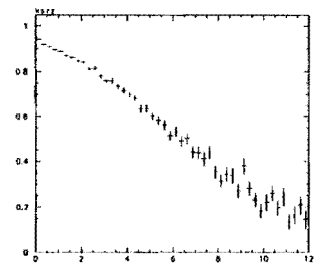

Figure 7.3: *Tracking efficiency as a function of d_0, the pion track impact parameter, with d_0 expressed in (cm).*

In Fig. 7.4 we show the P_T dependence of the tracking efficiency for π's from the K_S^0. The left and right plots only differ in the range of P_T displayed. The arrow on the left plot shows the minimum P_T for π's used in this analysis. The right plot shows a drop of the efficiency which is caused by the boost of the K_S^0 decay distance. This increase in the decay distance with P_T means that some K_S^0's will decay inside the CTC with the daughter π's crossing fewer wire layers.

We now proceed to show the B mass peak after retracking the event. In Fig. 7.5 we show the B peak for all tracks in the event with and without the requirement of

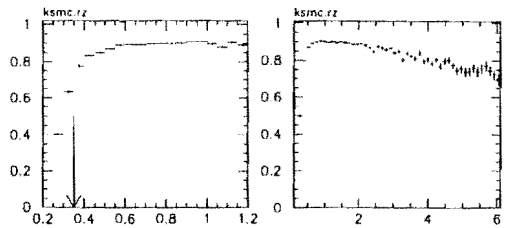

Figure 7.4: *Tracking efficiency as a function of $P_T(\pi)$. Left and right plot only differ in the P_T range. The arrow indicates the cut applied in the ratio of branching ratios measurement. The drop shown by the right plot is due to the boost in the K_S^0 decay distance with P_T.*

$(M(\pi^+\pi^-) - M(K_S^0))/\sigma < 3$. The tracking efficiency for reconstructing the K_S^0 for $P_T(K_S^0) > 1$ GeV/c and $P_T(\pi) > 0.35$ GeV/c is measured to be $87.4 \pm 1.0\%$ without a K_S^0 mass window and $85.8 \pm 0.5\%$ with a K_S^0 mass window.

7.4.1 Systematic Effect for the $J/\psi K_S^0$ Mode

This mode has an extra source of systematics due to the requirement of $(M(\pi^+\pi^-) - M(K_S^0))/\sigma < 3$. Presently at CDF there is some uncertainty as to the magnitude of the predicted track errors. To measure the impact of this uncertainty we scale the track errors and measure a change of about 1% in the efficiency. We assign a systematic of 1% to this effect.

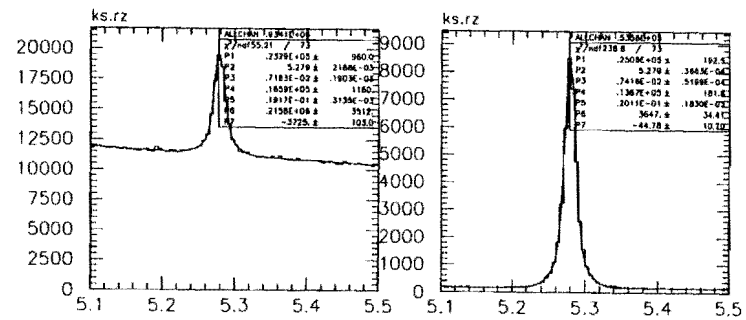

Figure 7.5: *Reconstructed B mass peak. Left plot uses all tracks in event while right plot requires $(M(\pi^+\pi^-) - M(K_S^0)/\sigma < 3$.*

7.4.2 Tracking Efficiency for the $J/\psi K_S^0$ Mode

We have measured the tracking efficiency for $P_T(K_S^0) > 1$ GeV/c, $P_T(\pi) > 0.35$ GeV/c to be 87.4 ± 1.0 (stat.) ± 1.7 (sys.)%.

Chapter 8

RECONSTRUCTION EFFICIENCIES

The measurement of the ratio of branching ratios requires us to determine the ratio of the reconstruction efficiencies between the modes (see Chapter 6). Here we will define the efficiencies needed and describe the method used to obtain them.

8.1 Monte Carlo Event Generator

Some of the efficiencies will have to be computed with a prediction of the b-quark P_T spectrum provided by a Monte Carlo generator [26, Chapter 5]. This code generates b-quarks with a P_T distribution determined from a next-to-leading order QCD calculation. This calculation has uncertainties originating from the b-quark mass, the renormalization scale and the structure functions. The b-quarks are generated in the rapidity region $-1.0 < y(b) < 1.0$ using the calculated correlation between the $P_T(b)$ and the rapidity distribution.

The generated b-quark is then fragmented into a B^+ or a B^0 according to the Peterson fragmentation function [38, Section 2.3]. The decay package **QQ** , developed

at CLEO, is used to force the decays $B^+ \to J/\psi K^+$, $B^0 \to J/\psi K^0_S$ and $J/\psi \to \mu^+\mu^-$. The $K^0_S \to \pi^+\pi^-$ decay is not forced at this stage. The decay package is set to model the expected polarization of the J/ψ.

8.2 Monte Carlo Sample

After the momenta of the B decay products have been generated, the detector response is simulated with **CDFSIM**. This package traces each particle through the detector until the particle stops or exits the detector volume. As the particle traverses the detector dE/dx and multiple scattering effects are simulated together with the information that the active regions of the detector are expected to generate. The $K^0_S \to \pi^+\pi^-$ decay is forced at this stage.

The simulated data are then processed with the same offline production package used for the Run-Ia data.

8.3 J/ψ Trigger Simulation

Even though the trigger efficiency for the J/ψ cancels in the ratio of efficiencies, we need to simulate the turn-on of the trigger in order to determine its effects on the spectra of the Kaon sector.

The trigger simulation used for this analysis parameterizes the responses of the Level 1 and Level 2 triggers as a function of the $P_T(\mu)$. It also implements the

algorithm described in Section 4.1.

The response of the Level 1 trigger was obtained by analyzing a data sample that passed a single muon trigger. The mass between the trigger muon and any other muon in the event was computed and J/ψ candidates were identified from the $M(\mu^+\mu^-)$ distribution. This second muon was then used to measure the turn-on of the efficiency of the Level 1 trigger. The efficiency of the Level 2 trigger was determined directly from the J/ψ data sample described in Chapter 4. The J/ψ trigger only requires one of the muon legs to pass the Level 2 trigger. The other muon can then be used to determine the Level 2 trigger efficiency [43].

The effect of the J/ψ trigger is considered by weighting each M.C. event by the probability of passing the trigger.

8.4 $J/\psi K^\pm$ Efficiency

The isolation procedure of the $B^\pm$ signal described in Section 5.6 determines the following string of efficiencies for the $J/\psi K^\pm$ mode

$$\epsilon = \epsilon_{P_T(B)} \times \epsilon_{cr(B)} \times \epsilon_{J/\psi} \times \epsilon_{P_T(K)} \times \epsilon_{R_E(K)} \times \epsilon_{\text{Tracking}} \times \epsilon_{\chi^2} \tag{8.1}$$

Not all the efficiencies in the formula above are needed as some of the terms cancel when taking the ratio of efficiencies between both modes. We now describe each term indicating which ones we cancel.

Efficiency of the $P_T(B) > 7$ GeV/c cut, $\epsilon_{P_T(B)}$

The $\epsilon_{P_T(B)}$ is the efficiency of the $P_T(B) > 7$ GeV/c cut. This efficiency cancels in the ratio because the same cut is applied to both modes.

Efficiency of detecting the J/ψ, $\epsilon_{J/\psi}$

Here $\epsilon_{J/\psi}$ is the efficiency of detecting the J/ψ. It includes the branching ratio $BR(J/\psi \to \mu^+\mu^-)$, the $P_T(\mu)$ cuts, the trigger efficiency, the μ tracking efficiency, and the μ geometrical acceptance. The $\epsilon_{J/\psi}$ cancels in the ratio of efficiencies but this ratio will have a residual dependency on these cuts through their influence on the P_T spectrum of the Kaon.

Efficiency of the $K^\pm$ selection, $\epsilon_{P_T(K)} \times \epsilon_{R_E(K)}$

The $\epsilon_{P_T(K)} \times \epsilon_{R_E(K)}$ is the $P_T(K^\pm)$ cut efficiency times the $K^\pm$ geometrical acceptance. The $\epsilon_{P_T(K)}$ cancels in the ratio because we apply the same cut on both modes. The $\epsilon_{R_E(K)}$ is determined from the M.C. sample by selecting all the events that satisfy the $P_T(B) > 7$ GeV/c, $P_T(\mu) > 1.8, 2.5$ GeV/c cuts and which have a reconstructed J/ψ, defined as a di-muon with mass within $\pm 3\sigma$ of the **P.D.G.** [50] value for $M(J/\psi)$. From these events we count all generated $K^\pm$'s from the B which satisfy the $R_E(K^\pm) > 86$ cm cut. The effect of the J/ψ trigger is considered by weighting each event by the probability of passing the trigger.

Efficiency of the $\mathrm{Prob}(\Delta\chi^2_F) > 0.01$ cut

The ϵ_{χ^2} is the efficiency of the $\mathrm{Prob}(\Delta\chi^2_F) > 0.01$ cut applied to the increment in χ^2_F after a new constraint has been added.

For the $J/\psi K^\pm$ mode it can be decomposed as

$$\epsilon_{\chi^2} = \epsilon_{V(\mu^+\mu^-)} \times \epsilon_{M(\mu^+\mu^-)} \times \epsilon_{V(K)} \times \epsilon_{Pxy(J/\psi K)} \times \epsilon_{Pz(J/\psi K)} \tag{8.2}$$

Here V refers to a vertex constraint, Pxy refers to a pointing constraint in the x-y plane and Pz refers to a pointing constraint in the z direction. In the ratio of efficiencies several of these efficiencies will cancel leaving us only to compute the reduced χ^2 efficiency

$$\epsilon^R_{\chi^2} = \epsilon_{V(K)} \tag{8.3}$$

We must also realize that the $J/\psi K^0_S$ mode has an equivalent term to $\epsilon_{V(K)}$ in the point constraints of the $\pi^+\pi^-$. We could think of $V(K)$ as two simultaneous point constraints of a charged track. So we take the ratio of efficiencies to be independent of the $\epsilon^R_{\chi^2}$ for the $J/\psi K^\pm$ mode. We will assign a systematic error to this assumption.

8.5 $J/\psi K^0_S$ Efficiency

The reconstruction efficiency for the $J/\psi K^0_S$ mode can be factorized as

$$\epsilon = \epsilon_{P_T(B)} \times \epsilon_{c\tau(B)} \times \epsilon_{J/\psi} \times \epsilon_{P_T(K^0_S)} \times$$

$$\epsilon_{K_S^0} \times \epsilon_{\text{Tracking}} \times \epsilon_{L_{xy}(K_S^0)} \times \epsilon_{d_\pi/\sigma_{d_\pi}} \times \epsilon_{\chi^2} \tag{8.4}$$

Efficiency of detecting the K_S^0, $\epsilon_{K_S^0}$

The $\epsilon_{K_S^0}$ is the K_S^0 detection efficiency and it includes the $P_T(\pi)$ cuts and the geometrical acceptance. We determine it from the M.C. by selecting all the events that satisfy the $P_T(B) > 7$ GeV/c, $P_T(\mu) > 1.8, 2.5$ GeV/c cuts and which have a reconstructed J/ψ, defined as a di-muon with mass within 3σ of the P.D.G. value. From these events we count all $\pi^+\pi^-$ from the K_S^0 which satisfy the $P_T(\pi) > 0.35$ GeV/c cut and have $R_E(\pi) > 86$ cm. We make sure these are the π's down the decay chain of the B as **CDFSIM** adds π's to the original event. We take into account the effect of the trigger efficiency by weighting each event by the probability of passing the trigger, computed with **MU2TRG**. We split this efficiency as

$$\epsilon_{K_S^0} = \epsilon_{R_E(\pi)} \times \epsilon_{P_T(\pi)} \tag{8.5}$$

Efficiency of the $L_{xy}(K_S^0) > 1.0$ cm cut

The efficiency for $L_{xy}(K_S^0) > 1.0$ cm is determined by embedding tracks in real data.

Efficiency of the $d_\pi/\sigma_{d_\pi} > 2$ cut, $\epsilon_{d_\pi/\sigma_{d_\pi}}$

Now we need the efficiency of the $d_\pi/\sigma_{d_\pi} > 2$ cut. We determine this efficiency

with the inclusive K_S^0 sample. We reconstruct a reasonably clean K_S^0 sample by computing the vertex constrained $M(\pi^+\pi^-)$ and requiring $L_{xy}(K_S^0) > 1.0$ cm and $d_K/\sigma_{d_K} < 4$ with d_K the K_S^0 impact parameter. We then plot the distribution of $M(\pi^+\pi^-)$ before and after applying the $d_\pi/\sigma_{d_\pi} > 2$ cut as it is shown in Fig. 8.1. We measure $\epsilon_{d_\pi/\sigma_{d_\pi}} = 87 \pm 2\%$ where the error is statistical.

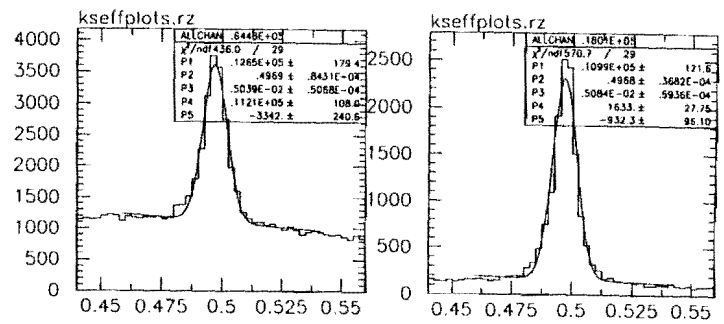

Figure 8.1: *Distribution of $M(\pi^+\pi^-)$ used to measure the efficiency of the $d_\pi/\sigma_{d_\pi} > 2$ cut. The left plot shows the distribution before the $d_\pi/\sigma_{d_\pi} > 2$ cut is applied while the right plot shows the distribution after the cut has been applied.*

Efficiency of the Prob$(\Delta\chi^2_F) > 0.01$ cut

The ϵ_{χ^2} is the efficiency of the Prob$(\Delta\chi^2_F) > 0.01$ cut applied to the increment in

χ^2_F after a new constraint has been added. For the $J/\psi K^0_S$ mode it can be decomposed as

$$\begin{aligned} \epsilon_{\chi^2} &= \epsilon_{V(\mu^+\mu^-)} \times \epsilon_{M(\mu^+\mu^-)} \times \\ &\epsilon_{V(\pi^+\pi^-)} \times \epsilon_{P(\pi^+\pi^-)} \times \epsilon_{M(\pi^+\pi^-)} \times \\ &\epsilon_{Pxy(J/\psi K^0_S)} \times \epsilon_{Pz(J/\psi K^0_S)} \end{aligned} \tag{8.6}$$

Here Pxy refers to a pointing constraint in the x-y plane and Pz refers to a pointing constraint in the z direction. In the ratio of efficiencies several of these efficiencies will cancel leaving us only to compute the reduced χ^2 efficiency

$$\epsilon^R_{\chi^2} = \epsilon_{V(\pi^+\pi^-)} \times \epsilon_{P(\pi^+\pi^-)} \times \epsilon_{M(\pi^+\pi^-)} \tag{8.7}$$

The cancellation of the $\mu^+\mu^-$ efficiencies does not deserve any comments. The cancellation of the efficiencies for the point constraints of the $J/\psi K^0_S$ system to the beam position against the efficiencies for the same constraints imposed on the $J/\psi K^\pm$ system is motivated from a study of the $J/\psi \to \mu^+\mu^-$ and the $\psi' \to J/\psi\pi^+\pi^-$ decays. It was observed that the efficiency of the Prob$(\Delta\chi^2_F) > 0.01$ cut was independent of the number of final tracks involved in the constraint.

The $J/\psi K^\pm$ mode has a term equivalent to the point constraint of the $\pi^+\pi^-$ in the χ^2_F when the $K^\pm$ track is added to the fit. The number of degrees of freedom is the same for both types of constraints and both constraints involve the requirement that the Kaon trajectory should go through the $\mu^+\mu^-$ secondary vertex. So we cancel

these terms in the ratio of efficiencies and then the $\epsilon^R_{\chi^2}$ only depends on the $\pi^+\pi^-$ Vertex and Mass constraints. Thus the only efficiency that we need to compute is

$$\epsilon^R_{\chi^2} = \epsilon_{V(\pi^+\pi^-)} \times \epsilon_{M(\pi^+\pi^-)} \tag{8.8}$$

We compute $\epsilon_{V(\pi^+\pi^-)}$ by using the inclusive K^0_S sample described earlier plus the $d_B(\pi)/\sigma_{d_B} > 2$ cut. We add this extra cut to reduce the background. If the errors were gaussian this cut should have an efficiency of 0.99, from this procedure we get $\epsilon_{V(\pi^+\pi^-)} = 0.98 \pm 0.02$ where the error is statistical.

We cannot apply the same procedure to compute $\epsilon_{M(\pi^+\pi^-)}$ because this constraint changes the distribution of $M(\pi^+\pi^-)$. Instead we fit the distribution of d_K/σ_{d_K} before and after the Prob$(\Delta\chi^2_F) > 0.01$ cut is applied. We measure $\epsilon_{M(\pi^+\pi^-)} = 0.99 \pm 0.02$.

Table 8.1: *Efficiencies for the $J/\psi K^{\pm}$ mode. The efficiencies have been computed for events that satisfy the $P_T(B) > 7$ GeV/c, $P_T(\mu) > 1.8, 2.5$ GeV/c cuts. The events are also required to have a reconstructed J/ψ.*

Cut	Efficiency Value
$R_E(K) > 86$ cm	0.980
Tracking	0.91

Table 8.2: *Efficiencies for the $J/\psi K^0_S$ mode. The efficiencies have been computed for events that satisfy the $P_T(B) > 7$ GeV/c, $P_T(\mu) > 1.8, 2.5$ GeV/c cuts. The events are also required to have a reconstructed J/ψ.*

Cut	Efficiency Value
$R_E(\pi) > 86$ cm	0.94
$P_T(\pi) > 0.35$ GeV/c	0.93
2 prev effs	0.873
Tracking	0.87
$L_{xy}(K^0_S) > 1$ cm	0.92
2 prev effs	0.80
$d_\pi/\sigma_{d_\pi} > 2$	0.87
Prob$(\Delta\chi^2_F) > 0.01$	0.97

Chapter 9

Systematic Uncertainties

This chapter discusses our study of systematic uncertainties for the ratio of branching ratios. We expect the systematics to be small because in the ratio of efficiencies several factors cancel. We will see that from all the possible source of systematic errors considered, only three contribute to the total systematic error of 6.4%.

9.1 $c\tau(B)$ cut

A simplifying assumption used is this analysis is to cancel the efficiencies for the $c\tau(B) > 0.01$ cm cut. Because the B^+ and the B^0 may have different lifetimes we need to assign a systematic error due to this assumption. In Ref. [26, Section 5.2.2] a method to estimate the $c\tau(B)$ cut efficiency is described. The method considers the B meson lifetime and the detector resolution to compute the efficiency from the convolution of an exponential (for the $c\tau(B)$ distribution) with a gaussian (to model the detector resolution). They conclude that an uncertainty of ~ 50 μm in the B lifetime produces a 2% uncertainty in the efficiency of the $c\tau(B)$ cut. We assign a 4%

systematic error to this source.

This systematic error should get reduced when a better measurement of the B^+ and B^0 lifetimes is available.

9.2 Tracking Efficiency

We use 0.87 ± 0.02 for the $J/\psi K^0_S$ mode and 0.91 ± 0.02 for the $J/\psi K^\pm$ mode. The quoted errors are upper bounds for the systematic uncertainties of the method used to measure it. We assign a 4% systematic error for the ratio of tracking efficiencies.

9.3 Monte Carlo $P_T(b)$ Spectrum

We study the effect of hardening and softening the default spectrum used by the monte carlo generator described in Section 8.1.

The two thick curves in Fig. 9.1 show two theoretical shapes available by changing the default b-quark mass and the renormalization scale. There is a significant variation of the absolute scales between the two curves but no significant change of the shape of the curves. Our measurement is not sensitive to a variation of the cross section scale because we are measuring a ratio but there could be some residual dependence on the shape given the different kinematics of the Kaon sector for the decay modes.

To study the dependence of our result on the $P_T(b)$ spectrum we produce two maximal variations of the theoretical shapes spectrum by multiplying or dividing the

spectrum by $(m_b^2 + P_T(b)^2)^{0.4}$. This factor is chosen because it approximately takes one curve into the other.

With these two maximal variations we compute the efficiencies shown in Table 9.1 only using quantities available at the generation level. We show the change in the $P_T(K^0_S)$ cut efficiency for completeness (the ratio does not depend on this efficiency). We see that the expected dependence is observed, that is, a harder $P_T(B)$ spectrum gives a higher efficiency for the $P_T(K^0_S)$ cut. There is no dependence of the other cuts on the $P_T(B)$ spectrum so we do not assign any systematic errors.

Table 9.1: *Effect of maximal $P_T(b)$ shape variations shown in Fig. 9.1.*

Cut	DEFAULT	SOFT	HARD
$P_T(K^0_S) > 1.5$ GeV/c	$67 \pm 1\%$	$64 \pm 1\%$	$71 \pm 1\%$
$P_T(\pi) > 0.35$ GeV/c	$92 \pm 1\%$	$91 \pm 1\%$	$92 \pm 1\%$
$L_{xy}(K^0_S) > 1$ cm	$94 \pm 1\%$	$94 \pm 1\%$	$91 \pm 1\%$

9.4 Trigger Systematics

We investigate the effect of the uncertainties of the trigger model on our ratio of efficiencies. We select high/low efficiency curves for the Level 1 trigger and the Level 2 trigger. We do not observe any significant variation. We must point out that we

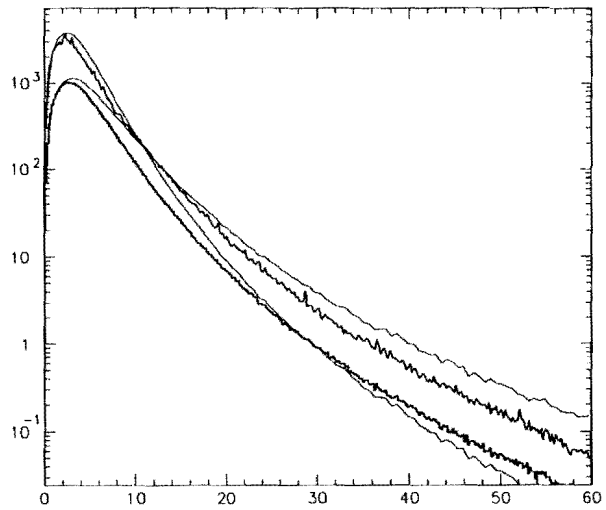

Figure 9.1: *Maximal variations of the default $P_T(b)$ spectrum used in this analysis. The two thick curves are obtained by changing the default b-quark mass and the renormalization scale. The thin curves show the variations obtained by multiplying or dividing the spectrum by $(m_b^2 + P_T(b)^2)^{0.4}$. This factor is chosen because it approximately takes one theory curve into the other.*

have changed the turn-on curves according to the uncertainty of the CMU curves.

The uncertainties for the CMX system are larger and are treated independently. We change the Level 1 CMX trigger turn-on maximally and again we find no dependence of our efficiencies on the trigger model.

We must point out that we found no dependence of the individual efficiencies. This indicates that the Kaon P_T spectrum is insensitive to the uncertainties of the trigger turn-on.

9.5 Pion Impact Cut

We study a possible systematic error coming from the $P_T(K_S^0)$ spectrum into the measurement of the pion impact cut efficiency. We are concerned that harder K_S^0's may have a larger d_π distribution and thus a higher efficiency. We apply different $P_T(K_S^0)$ cuts and measure the efficiency. The results are given in Tab. 9.2. No dependence can be seen. This could mean a cancellation between two competing effects related to the boost. One is the loger decay length of boosted K_S^0's which results in larger π impact parameters. The other effect is the decrease of the $\pi^+\pi^-$ opening angle which results in smaller π impact parameters.

Table 9.2: *Efficiency of $d_\pi/\sigma_{d_\pi} > 2$ cut for different values of $P_T(K_S^0)$.*

$P_T(K_S^0) >$ GeV/c	eff
0.0	0.87 ± 0.02
1.0	0.88 ± 0.02
1.5	0.89 ± 0.02
2.0	0.87 ± 0.02
3.0	0.86 ± 0.02

9.6 P_T Dependence of the Probability Cut

We are concerned with a possible anomalous P_T dependence of the tracking errors. A study performed on the J/ψ normalized mass [44] indicates that the width of the distribution has a slight dependence on the P_T of the μ tracks.

To study the effect of this dependence on our $\text{Prob}(\Delta\chi^2_F) > 0.01$ cut we split the K_S^0 sample according to the P_T of the softest π. We cut at 0.65 GeV/c trying to split the sample in halves. In Table 9.3 we show the resulting efficiency for the vertex constrain cut. In Table 9.4 we show the resulting efficiency for the mass constrain cut.

The change is minimal when compared to the statistical error. We assign no systematic error to this effect.

Table 9.3: *Study of $P_T(\pi)$ dependence of the efficiency of the $\text{Prob}(\Delta\chi^2_F) > 0.01$ cut for the vertex constraint. The error is statistical.*

$P_T(\pi)$	eff
< 0.65 GeV/c	$97 \pm 2\%$
> 0.65 GeV/c	$98 \pm 2\%$

Table 9.4: *Study of $P_T(\pi)$ dependence of the efficiency of the $\text{Prob}(\Delta\chi^2_F) > 0.01$ cut for the mass constraint. The error is statistical.*

$P_T(\pi)$	eff
< 0.65 GeV/c	$99 \pm 2\%$
> 0.65 GeV/c	$99 \pm 2\%$

9.7 Dependence on P_T Cuts

To get an idea of the dependence or our result on the P_T cuts applied to the B and the Kaons we show in Table 9.5 the ratio of branching ratios obtained with different P_T cuts. The last column shows the variations of the result when compared to the value 0.77. The number of events and the efficiencies are slightly different from the final values used in our measurement because they were determined in a different manner. We conclude that the variations are well within the statistical uncertainty

of the measurement. We assign no systematic error to these selection cuts.

Table 9.5: *Dependence of the BR/BR on the $P_T(B)$ and Kaon P_T cuts. Values of the P_T cuts are in units of GeV/c. Errors in the BR/BR are statistical only.*

$J/\psi K^{\pm}$		$J/\psi K^0_S$		$\frac{N(Bu)}{N(Bd)}$	BR/BR	Δ
$P_T(B)$	$P_T(K^{\pm})$	$P_T(B)$	$P_T(K^0_S)$			
6	1	6	1	174/45	.77 ± .15	0.00
6	1.5	6	1.5	150/41	.80 ± .16	0.03
6	2	6	2	108/29	.85 ± .19	0.08
6	2.5	6	2.5	83/23	.88 ± .23	0.11
6	3	6	3	71/22	.79 ± .20	0.02
7	1	7	1	137/40	.78 ± .16	0.01
7	1.5	7	1.5	132/37	.77 ± .16	0.00
7	2	7	2	104/30	.78 ± .18	0.01
7	2.5	7	2.5	83/23	.85 ± .24	0.08
7	3	7	3	71/22	.79 ± .22	0.02
8	1	8	1	124/37	.76 ± .16	-0.01
8	1.5	8	1.5	118/34	.74 ± .16	-0.03
8	2	8	2	96/27	.79 ± .18	0.02
8	2.5	8	2.5	80/22	.86 ± .23	0.09
8	3	8	3	70/22	.77 ± .19	0.00

9.8 Fitting Procedure

We investigate the effect of two parts of our fitting procedure on the $N(J/\psi K^{\pm})/N(J/\psi K^{0}_{S})$ ratio: the fitting function and the width of the gaussian used to model the signal.

9.8.1 Integrate Across the Bin

As explained in Section 6.2 the number of signal events is only approximately given by the parameter N_S, the exact value given by a sum like the one shown in Eq. 6.5.

An alternative procedure is to fit the function

$$\tilde{f}(m) = N_S \times (\mathrm{freq}(\hat{m} + \frac{\mathrm{bw}}{2\sigma}) - \mathrm{freq}(\hat{m} - \frac{\mathrm{bw}}{2\sigma})) + N_B \times \frac{\mathrm{bw}}{5\sigma} \tag{9.1}$$

which is obtained by using Eq. 6.5 for only one bin. Here $\hat{m} \equiv (m - \mu)/\sigma$ and freq is the **CERN** library function defined as

$$\mathrm{freq}(x) = \frac{1}{\sqrt{2\pi}} \int_{-\infty}^{x} \exp(-\frac{t^2}{2}) dt \tag{9.2}$$

The difference between fitting f and $\tilde{f}$ is that the parameter N_S now truly represents the number of signal events. The fit is shown in Fig. 9.2.

9.8.2 Float the Width of the Gaussian

For our result we fix the width of the gaussian to 1. In Fig. 9.3 we show the effect of letting the width float (the function fitted is f). The fitted width is given by parameter P3.

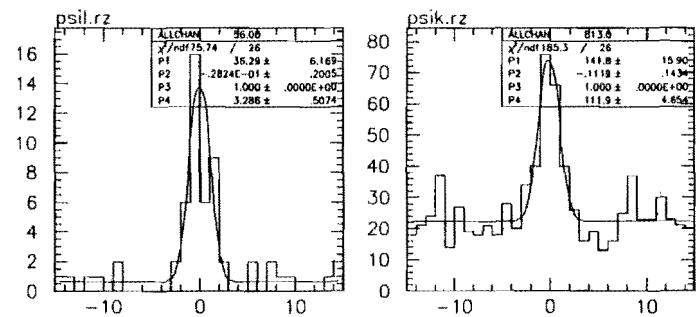

Figure 9.2: *Fit using function $\tilde{f}$, which is described in the text. The number of events is given by parameter P1.*

9.8.3 Results

In Table 9.6 we summarize the ratio of the number of events from the three procedures reported in this thesis. We do not assign a systematic uncertainty to the fitting procedure because the changes are well contained within the statistical errors.

Table 9.6: *Dependence of the ratio of observed events with the fitting procedure. The ratio is* $N(J/\psi K^{\pm})/N(J/\psi K^{0}_{S})$.

Method	$N(J/\psi K^{0}_{S})$	$N(J/\psi K^{\pm})$	Ratio
Fit f	36.0 ± 6.4	139.3 ± 15.7	3.87 ± 0.82
Fit $\tilde{f}$	36.3 ± 6.2	141.8 ± 15.9	3.91 ± 0.83
Float σ	37.1 ± 6.5	145.2 ± 17.8	3.91 ± 0.83

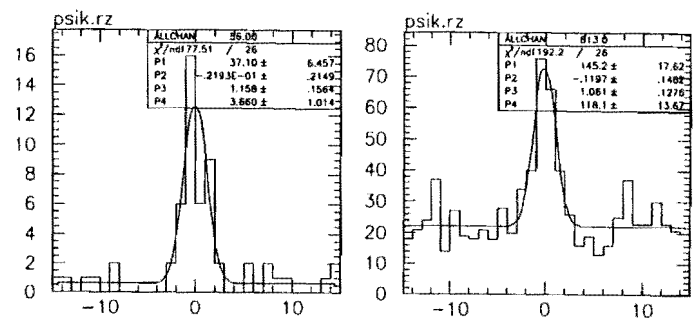

Figure 9.3: *Fit with a floating width. The number of events is given by parameter P1 and the width by parameter P3.*

9.9 Cancellation of $\mathrm{Prob}(\Delta\chi^2_F) > 0.01$

We have assumed the following cancellation of efficiencies

$$\frac{\epsilon_{P(\pi^+\pi^-)} \times \epsilon_{Pxy(J/\psi K^0_S)} \times \epsilon_{Pz(J/\psi K^0_S)}}{\epsilon_{V(K)} \times \epsilon_{Pxy(J/\psi K)} \times \epsilon_{Pz(J/\psi K)}} \tag{9.3}$$

As it was indicated in Section 8.5, the cancellation of the efficiencies for the point constraints of the two B systems is expected to hold as a result of the independence of the efficiency of the $\mathrm{Prob}(\Delta\chi^2_F) > 0.01$ cut with respect to the number of tracks involved in the constraint.

We now check whether the cancellation of the efficiencies for the $P(\pi^+\pi^-)$ and $V(K)$ constraints holds in the M.C. sample. This is necessary because these two constraints are treated differently by the algorithm. The constraint of the K^0_S is treated as a point constraint while the $K^\pm$ is treated as a vertex constraint. In Fig. 9.4 we show the distribution of $\Delta\chi^2_F$ when the $K^\pm$ is added or when the K^0_S is point constrained in 3D. The fit shown is a χ^2 distribution with 2 dof and a scaling factor given by parameter P2. We only fit the region 0-14 to avoid the tails coming from non-gaussian errors. We conclude that the shapes are consistent with each other.

We know proceed to compute the efficiency for the $\mathrm{Prob}(\Delta\chi^2_F) > 0.01$ cut. To do this we count the number of events within $\pm 2.5\sigma$ in the normalized $M(B)$ distribution before and after applying the cut. We measure $\epsilon_{P(\pi^+\pi^-)} = 0.962 \pm 0.002$ and $\epsilon_{V(K)} = 0.967 \pm 0.002$. The errors are binomial.

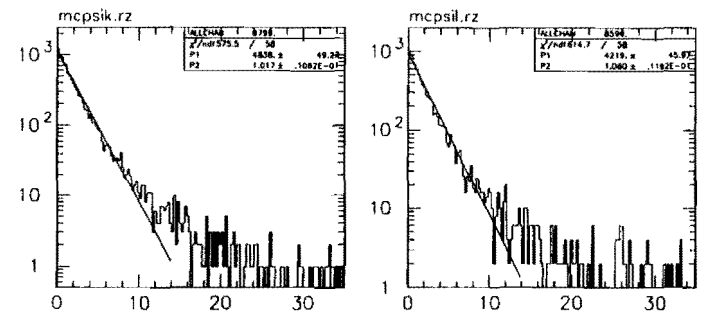

Figure 9.4: *Distribution of $\Delta\chi^2_F$ when the $K^\pm$ is added (left) or when the K^0_S is point constrained in 3-D (right). The fitted scaling factor is P2. The fitted values are fairly consistent.*

If the smearing of measured quantities were gaussian, this cut would be 99% efficient. The M.C. predicts only a 96% efficiency. We assign a 3% systematic error -as an upper limit- to the cancellation of the efficiencies of the Prob($\Delta\chi^2_F$) > 0.01 cuts.

9.10 Summary of Systematics

In Table 9.7 we summarize the values used in this analysis for the systematic error estimates.

Table 9.7: *Values for the systematics associated with this measurement.*

Origin	Value (%)
$c\tau(B) > 0.01$ cm	4
Tracking Efficiency	4
Prob > 0.01	3
combined	6.4

Chapter 10

RESULTS AND CONCLUSIONS

The measured ratio of the numbers of events is obtained from the fitted values shown in Table 6.1

$$\frac{N(J/\psi K^{\pm})}{N(J/\psi K^0_S)} = 3.87 \pm 0.82 \text{ (stat.)} \tag{10.1}$$

The error quoted represents a 21% statistical error and it is the dominant uncertainty of the measurement.

The ratio of efficiencies is determined from Tables 8.1 and 8.2, namely we have

$$\begin{aligned}
\frac{\epsilon_{J/\psi K^0_S}}{\epsilon_{J/\psi K^{\pm}}} &= \left(\epsilon_{R_E(\pi)} \times \epsilon_{P_T(\pi)}\right) \times \\
&\quad \frac{\left(\epsilon_{\text{Tracking}} \times \epsilon_{L_{xy}(K^0_S)}\right) \times \epsilon_{d_x/\sigma_{d_x}} \times \epsilon^{R}_{\chi^2}}{\epsilon_{R_E(K)} \times \epsilon_{\text{Tracking}}} \\
&= 0.873 \times \frac{0.80 \times 0.87 \times 0.97}{0.980 \times 0.91} \\
&= 0.661 \pm 0.042 \text{ (sys.)}
\end{aligned} \tag{10.2}$$

The systematic error corresponds to the 6.4% from Table 9.7. This ratio of efficiencies needs to be corrected for the branching ratio $BR(K^0_S \to \pi^+\pi^-)$ because we forced

this decay mode during simulation. So using Eq. 6.3 we get

$$\begin{aligned}\frac{BR(B^+ \to J/\psi K^+)}{BR(B^0 \to J/\psi K^0)} &= \frac{1}{2}\frac{N(J/\psi K^+)}{N(J/\psi K_S^0)} \times \frac{\epsilon_{B^0}}{\epsilon_{B^+}} \times BR(K_S^0 \to \pi^+\pi^-) \\ &= 0.5 \times (3.87 \pm 0.82) \times (0.661 \pm 0.042) \times 0.686 \\ &= 0.88 \pm 0.18\ (\text{stat.}) \pm 0.06\ (\text{sys.}) \qquad (10.3)\end{aligned}$$

We now use the **CLEO** value for $BR(B^+ \to J/\psi K^+)$ from Ref. [3] to obtain

$$BR(B^0 \to J/\psi K^0) = 0.125 \pm 0.031\ (\text{stat.}) \pm 0.014\ (\text{sys.})\ \% \qquad (10.4)$$

10.1 Comparison to other $\tau(B^+)/\tau(B^0)$ Measurements and Theory

We have collected in Table 10.1 a list of recent measurements of the $\tau(B^+)/\tau(B^0)$ ratio. All CDF measurements refer to the same run. We can see that our measurement is consistent with all other measurements within our statistical errors. We can also see that our measurement is consistent with the prediction available in Ref. [2] which gives

$$\frac{\tau(B^+)}{\tau(B^0)} \simeq 1 + 0.05\frac{f_B^2}{(200\ \text{MeV})^2} \qquad (10.5)$$

where f_B is the B meson decay constant. Using an estimated value of [19, Table 12] $f_B \approx 180 \pm 50$ MeV the ratio is expected to exceed 1.0 by a few percent to 10 percent.

Table 10.1: *A summary of recent ratio of lifetimes measurements.*

Experiment	Technique	$\tau(B^+)/\tau(B^0)$
CDF	$BR(B^+ \to J/\psi K^+)/BR(B^0 \to J/\psi K^0)$	$0.88 \pm 0.18 \pm 0.06$
CLEO [45]	$BR(B^+ \to Xl\nu)/BR(B^0 \to Xl\nu)$	$0.93 \pm 0.18 \pm 0.12$
OPAL [46]	Dl	$0.99 \pm 0.14^{+0.05}_{-0.04}$
DELPHI [47]	Event Topology	$1.06^{+0.13}_{-0.11} \pm 0.10$
DELPHI [48]	$\bar{D}l^+$	$1.00^{+0.17}_{-0.15} \pm 0.10$
CDF [6]	$J/\psi K$ Direct	$1.02 \pm 0.16 \pm 0.06$
CDF [49]	Dl	$0.96 \pm 0.10 \pm 0.05$

10.2 Comparison to Other Exclusive Branching Ratio Measurements and Theory

In this Section we compare our results to other experiments which use the same exclusive channels to compute the branching ratios for $J/\psi K^\pm$ and $J/\psi K_S^0$. We only compare to CLEO II, given that their statistics far surpass the other experiments. We can see that our measurement of the ratio of branching ratios has the best statistical error (20% compared to 35%), this is expected as CLEO only reports 10.0 ± 3.2 events for the $J/\psi K_S^0$ mode. We then compare our measurement for $BR(B^0 \to J/\psi K^0)$. The CDF statistical error now increases up to 25% because we use the CLEO value for

$BR(B^+ \to J/\psi K^+)$. This statistical error is comparable to the 32% statistical error for CLEO's measurement of $BR(B^0 \to J/\psi K^0)$.

Table 10.2: *Branching ratios measurement available at present for the exclusive decay channels. The values for ARGUS, CLEO 1.5 and CLEO II were taken from Ref. [11]. P.D.G. 1994 refers to the world average value given in Ref. [50].*

Source	$BR(B^+ \to J/\psi K^+)$ %	$BR(B^0 \to J/\psi K^0)$ %	Ratio
CDF		$0.125 \pm 0.031 \pm 0.014$	$0.88 \pm 0.18 \pm 0.06$
ARGUS	0.08 ± 0.04	0.09 ± 0.07	0.89 ± 0.82
CLEO 1.5	0.09 ± 0.03	0.07 ± 0.04	1.3 ± 0.9
CLEO II	$0.110 \pm 0.015 \pm 0.009$	$0.075 \pm 0.024 \pm 0.008$	$1.47 \pm 0.51 \pm 0.20$
P.D.G. 1994	0.102 ± 0.014	0.075 ± 0.021	1.36 ± 0.42

From Ref. [51] we obtain a prediction based on the factorization approach. The method uses results from ARGUS and CLEO to fit an effective parameter a_2. The modes used in the fit are $B^0 \to J/\psi K^0_S$, $J/\psi K^{*0}$ and $B^+ \to J/\psi K^+$, $J/\psi K^{*+}$. The result is $|a_2| = 0.26 \pm 0.01 \pm 0.01 \pm 0.02$, where the first error is statistical, and the second and third are systematic. The prediction of

$$BR(B^0 \to J/\psi K^0) = 1.817 a_2^2 \% \tag{10.6}$$

can be used to get

$$BR(B^0 \to J/\psi K^0) = 0.123 \pm 0.02\% \tag{10.7}$$

where the error is the combined error in quadrature from the a_2 uncertainties.

We can see that there is very good agreement with our measurement. This agreement should be taken with caution. As stated in Ref. [51], the factorization assumption is not well founded for colour suppressed decays.

10.3 Future Prospects

In Table 10.3 we list the three sources of uncertainties for the ratio of branching ratios measurement. We see that the main uncertainty in our measurement comes from the low statistics of the $J/\psi K^0_S$ mode. Improving this value is not an easy task, though. In Fig. 10.1 we show a $J/\psi K^0_S$ peak obtained with the same data but with looser selection cuts. We see that the signal has increased to be 55 ± 9 events. The statistical error now is $9/55*100 = 16\%$ not the naively expected $\approx \sqrt{55}/55*100 = 13\%$. The correct formula to use for the uncertainty in the number of events S is $\sigma \approx \sqrt{S+B}$ with B the number of background events under the peak. This means that if we relax the cuts to get more signal, the improvement gets diluted by the corresponding increment of the background.

In this analysis we have kept the cuts applied to each mode as similar as possible in order to keep a better control of systematic uncertainties and possible errors in the

computations. This means that if we gain $J/\psi K_S^0$ events by loosening some cuts, we will get a worse signal-to-noise ratio in the $J/\psi K^\pm$ mode. This leads us to conclude:

- The most obvious improvement to the present measurement will come from the added data from the ongoing run (Run-Ib) with an expected total luminosity of 100 pb^{-1} by the end of July 1995. This will mean that our statistical error should reduce from 20% down to 10% once the whole data set is analyzed. The statistical uncertainty of the branching ratio measurement should decrease from 25% down to 17% (we have kept the present CLEO uncertainty of 14%).

Table 10.3: *Sources of uncertainties for the ratio of branching ratio measurement.*

Source	Contribution %
$N(J/\psi K_S^0)$	18
$N(J/\psi K^\pm)$	11
Systematic	6.4

The three B decay modes reconstructed in this thesis show very different signal-to-noise ratios. The $J/\psi K^\pm$ has $S/N \approx 1.0$, the $J/\psi K^{*\pm}$ has $S/N \approx 5.0$ and the $J/\psi K_S^0$ has $S/N \approx 10.0$. This is indicating that the identification of Kaons in a hadronic environment is an important issue to reduce background. We already pointed out in

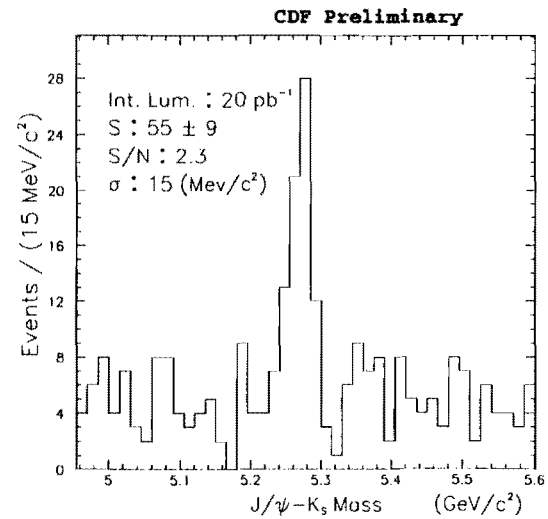

Figure 10.1: *Mass plot for $J/\psi K_S^0$ mode showing 55 ± 9 events. The statistical error is 16% because of the increase in the background. Without background the statistical error would be 13%.*

Chapter 1 that the Fermilab Tevatron has a b-quark production cross section that is 50,000 times larger than a e^+e^- collider working at the $\Upsilon(4S)$ resonance (at the energy of LHC, $\sqrt{s} = 16$ TeV, the cross section is about 500,000 times larger). This fact would make a hadron collider the ideal place to study B physics were it not for the very large backgrounds that have to be rejected. A particle ID system capable of differentiating Kaons from pions in the P_T range $1.0 < P_T < 2.0$ GeV/c could prove useful to improve the S/N of the $J/\psi K^{\pm}$ mode.

The CDF silicon vertex detector has proven to be a very important element of this analysis by allowing us to lower the P_T cuts while keeping a good signal-to-noise ratio. During Run-Ia the SVX suffered radiation damage, mainly from 30 pb^{-1} of collisions, which lowered its performance [27]. The main effects of this dose are an increment of the leakage currents of the SVX ladders, an increase of the electronics noise and a decrease of the gain of the readout chip installed in the SVX detector. For Run-Ib an AC-coupled detector (SVX′) equipped with a radiation-hard readout chip was installed in its place. The SVX′ is expected to survive the radiation damage from a few hundred pb^{-1} of data at the Tevatron. An important drawback is that the SVX only covered about 70% of the interaction region. This means that only about 60% of the J/ψ's have both muon legs in the SVX, which reduces the impact of the SVX. For Run-Ib a small improvement was obtained by a change in the design that eliminated a small gap between the two barrels with a consequent 5% increase in the

acceptance. A longer detector (SVX-II) consisting of three barrels will be in place for Run-II (scheduled for the end of 1998) with a total length of 96 cm (compared to 51 cm of the SVX and SVX′ detectors). Another important feature of the SVX-II is that it has 3D tracking capabilities.

Two assumptions were needed in the measurements reported in this thesis. The first one (Chapter 6) is that the production of neutral and charged B mesons is the same, namely

$$\sigma(\bar{p}p \to \bar{b} \to B^+) = \sigma(\bar{p}p \to \bar{b} \to B^0) \tag{10.8}$$

This assumption has been used in published results and it is expected to hold at CDF. The second assumption refers to the equal rates for the partial decay rates (see the Introduction):

$$\Gamma(B^+ \to J/\psi K^+) = \Gamma(B^0 \to J/\psi K^0) \tag{10.9}$$

In the future when an increased number of reconstructed events allows for a significant reduction of the statistical error we should consider measuring the following ratios instead:

$$\begin{aligned} R_+ &\equiv \frac{BR(B^+ \to J/\psi K^{*+})}{BR(B^+ \to J/\psi K^+)} \\ R_0 &= \frac{BR(B^0 \to J/\psi K^{*0})}{BR(B^0 \to J/\psi K^0)} \end{aligned} \tag{10.10}$$

These ratios can be used to check the validity of the factorization hypothesis for this type of decays. Neither of the two assumptions mentioned above are needed for these ratios.

The main interest in the $J/\psi K_S^0$ mode comes from being the "golden mode" for the study of CP violation. In Appendix A.5 we show the several simplifications that this mode permits for the measurement of the angle β of the unitarity triangle. This thesis demonstrates that it is possible to reconstruct a very clean $J/\psi K_S^0$ sample in a hadronic environment. Based on this result an expression of interest by CDF has been submitted to Fermilab that expects to measure $\sin(2\beta)$ with a ± 0.18 uncertainty by the end of year 1999 with a total integrated luminosity of 1.5 fb^{-1}. Four basic improvements over the present CDF performance are expected to make this measurement possible. The decay mode $J/\psi \to e^+e^-$ is expected to improve detection rates by a factor of two. The planned upgrade of the Data Acquisition System (DAQ) for Run-II will permit lowering the muon P_T trigger thresholds to 1.5 GeV/c (for Run-Ib the present DAQ cannot handle the trigger rate resulting in physics events getting lost). A Time of Flight system is being proposed to provide Kaon/pion separation of 2σ up to 1.6 GeV/c. This should improve the efficiency to detect the other B in the event. The tracking and triggering acceptance would need to be improved also.

The expected asymmetry if the CKM phase is responsible for CP violation is expected to be [52] $0.53 \leq \sin 2\beta \leq 0.81$, which means CP violation outside the Kaon system could be observed in an upgraded version of CDF by the year 2000.

Appendix A

CP VIOLATION

About 30 years ago (1964) Christenson *et al.* [14] reported the observation of the CP violating decay $K_L^0 \to \pi^+\pi^-$. The $\pi^+\pi^-$ can only have CP = 1 [19, Section VI.B]. The K_L^0 is an eigenstate of the total Hamiltonian. If the Hamiltonian conserved CP then K_L^0 would have CP = -1 and the decay would be forbidden.

There is no solid theoretical understanding of the origin of CP violation. The experimental observations thus far could be completely due to the $K_L^0(K_S^0)$ being almost CP = $-1(+1)$ eigenstates with a small ($\sim \bar{\epsilon}$) mixture of the other CP eigenstate. The Standard Model (S.M.) allows for this situation but the predictions have large uncertainties. The observation of direct CP violation (defined later) would rule out a class of models called *superweak* and could provide support for the S.M. The modes $B^0 \to J/\psi K_S^0$ together with $B^0 \to \pi^+\pi^-$ serve as a good probe of direct CP violation [15, Section VIII.B].

The measurement of CP asymmetries in B decays can also provide checks on

physics beyond the S.M.. This could happen in several ways [16]:

1. Significant contributions from new physics to B-$\bar{B}$ mixing.

2. Unitarity of the CKM matrix does not hold.

3. Decays where the expected S.M. asymmetry is small (like penguin dominated decays), if measured to be large, would signal new physics.

The study of CP violation may also have relevance to explain the baryon asymmetry in the Universe. The present observed ratio between the nucleon density n_N and photon density n_γ is [17, Eq. 14.67]:

$$\frac{n_N}{n_\gamma} \approx 10^{-9} \tag{A.1}$$

This density is computed from the 2.7 K degree background blackbody radiation. This radiation can be traced back in time to mean that about 10^{-7} sec after the origin of the Universe there was an asymmetry between the quark density and the anti-quark density of

$$\delta = \frac{n_q - n_{q^c}}{n_q + n_{q^c}} \approx 10^{-9} \tag{A.2}$$

Within the context of the S.M. this cosmological asymmetry can only be introduced as an initial boundary condition, which seems unesthetic. An alternative path is to postulate an interaction (beyond the S.M.) which would dynamically generate the asymmetry around 10^{-33} sec into the Big-Bang. This new interaction would have to violate CP [18].

A.1 CKM Matrix

The following discussion is taken from Ref. [18]. In the minimal S.M. the Yukawa interaction is written as [18, formula (2.142)]

$$\mathcal{L}_{\rm Yuk} = \sum_{mn=1}^{F} \Gamma^u_{mn} \bar{q}^0_{mL} \tilde{\varphi}\, u^0_{nR} + \sum_{mn=1}^{F} \Gamma^d_{mn} \bar{q}^0_{mL} \varphi\, d^0_{nR} + \sum_{mn=1}^{F} \Gamma^e_{mn} \bar{l}^0_{mL} \varphi\, e^0_{nR} + \text{H.C.} \tag{A.3}$$

where Γ^u, Γ^d and Γ^e are arbitrary $F \times F$ matrices, m, n are indexes that run across the F families. The symbols $\bar{q}^0_{mL}$ and $\bar{l}^0_{mL}$ represent the SU(2) doublets of left-handed fermions

$$q^0_{mL} = \begin{pmatrix} u^0_m \\ d^0_m \end{pmatrix}_L \tag{A.4}$$

$$l^0_{mL} = \begin{pmatrix} \nu^0_m \\ e^0_m \end{pmatrix}_L \tag{A.5}$$

The superscript 0 denotes "weak interaction basis", that is, the basis where the currents are flavor-diagonal [19, page 126]. The symbol φ represents the doublet of scalar particles

$$\varphi = \begin{pmatrix} \varphi^+ \\ \varphi^0 \end{pmatrix} \tag{A.6}$$

and

$$\tilde{\varphi} = \begin{pmatrix} \varphi^{0\dagger} \\ -\varphi^- \end{pmatrix} \tag{A.7}$$

H.C. means hermitian conjugate.

The condition that only the left-handed fermions transform under the SU(2) gauge transformations forbids the inclusion of bare fermion mass terms. The fermion masses are generated through spontaneous symmetry breaking by which the neutral component of the Higgs field φ acquires a vacuum expectation value (here taken to be real and of magnitude $\nu/\sqrt{2}$). From Eq. A.3 we can see this V.E.V. induces the following terms in the Lagrangian

$$\begin{aligned}\mathcal{L}_M &= \sum_{mn=1}^{F} \bar{u}^0_{mL}\Gamma^u_{mn}\frac{\bar{\nu}}{\sqrt{2}}u^0_{nR} + \sum_{mn=1}^{F} \bar{d}^0_{mL}\Gamma^d_{mn}\frac{\nu}{\sqrt{2}}d^0_{nR} + \sum_{mn=1}^{F} \bar{e}^0_{mL}\Gamma^e_{mn}\frac{\nu}{\sqrt{2}}e^0_{nR} + \text{H.C.} \\ &= \bar{u}^0_L M^u u^0_R + \bar{d}^0_L M^d d^0_R + \bar{e}^0_L M^e e^0_R + \mathbf{H.C.} \qquad \text{(A.8)}\end{aligned}$$

The mass matrixes $M^{u(d,e)}$ are in general complex and non-hermitian. A unitary transformation of the fields can be used to make them diagonal by expressing the Lagrangian in terms of the "mass eigenstate basis" of fermion fields, namely

$$u^0_L \equiv A^u_L u_L \qquad \text{(A.9)}$$

$$u^0_R \equiv A^u_R u_R \qquad \text{(A.10)}$$

with similar transformations for the d^0's and e^0's. The electromagnetic and neutral weak currents do not change form in this new basis. The leptonic part of the charged weak current does not change form either because the neutrinos are supposed to be massless. The part dealing with quarks generates interaction terms between fields from different families according to

$$\sum_{mn=1}^{F} 2\bar{d}_m P_L A_{Cmn} u_n \qquad \text{(A.11)}$$

with P_L the projection operator into left-handed fields and

$$A_C \equiv A^{d\dagger}_L A^u_L \qquad \text{(A.12)}$$

is the generalized Cabibbo matrix. In the case of $F = 3$ this matrix is referred to as the Cabibbo-Kobayashi-Maskawa matrix (from now on V). The CKM matrix has enough degrees of freedom to contain an imaginary number whose phase is observable. The matrix can be written [20, page 1633]

$$V = \begin{pmatrix} V_{ud} & V_{us} & V_{ub} \\ V_{cd} & V_{cs} & V_{cb} \\ V_{td} & V_{ts} & V_{tb} \end{pmatrix} \simeq \begin{pmatrix} 1 & \lambda & A\lambda^3(\rho - i\eta) \\ -\lambda & 1 & A\lambda^2 \\ A\lambda^3(1-\rho-i\eta) & -A\lambda^2 & 1 \end{pmatrix} \qquad \text{(A.13)}$$

The second expression is known as the Wolfenstein's parameterization. The expansion in powers of the "small" parameter λ ($\lambda = 0.22$) is motivated by the observed hierarchical structure of the couplings. The possibility of having $\eta \neq 0$ allows us to have a CP violating interaction in the S.M.

With this definition the part of the Lagrangian providing interactions across families can be written as [21]

$$\mathcal{L}^{\text{CKM}}_{\text{Int}} = \frac{g}{\sqrt{2}}\{(\bar{u}\ \bar{c}\ \bar{t})_L\gamma^\mu V \begin{pmatrix} d \\ s \\ b \end{pmatrix}_L W^+_\mu + (\bar{d}\ \bar{s}\ \bar{b})_L\gamma^\mu V^\dagger \begin{pmatrix} u \\ c \\ t \end{pmatrix}_L W^-_\mu\} \qquad \text{(A.14)}$$

A.2 The Unitarity Triangle

The CKM matrix defined by Eq. A.12 is unitary. This condition is commonly represented geometrically in terms of triangles as shown in Fig. A.1 for the relation

$$V_{ud}V_{ub}^* + V_{cd}V_{cb}^* + V_{td}V_{tb}^* = 0 \tag{A.15}$$

rescaled by $V_{cd}V_{cb}^*$ [20]. The angle β can be expressed as

$$\beta = \arg(-\frac{V_{cd}V_{cb}^*}{V_{td}V_{tb}^*}) \tag{A.16}$$

with similar expressions for α and γ. These three angles can be directly related to CP violating asymmetries in the decay rates for quark transitions shown in Fig. A.1. We will show later how the decay mode $B_d \to J/\psi K_S^0$ can determine the angle β.

A.3 B^0-$\bar{B}^0$ Mixing

The fact that the strong interaction dominates the production of hadrons allows one to produce states which are exclusively eigenstates of the strong interactions but not of the total Hamiltonian. Degenerate states of the strong interaction can be coupled by the weak interaction which can connect quarks across families. Example of these systems are $\{K^0,\bar{K}^0\}$, $\{D^0,\bar{D}^0\}$, $\{B^0,\bar{B}^0\}$. The coupling among degenerate states means that a pure initial $|B^0>$ state will have a $|\bar{B}^0>$ component after the system evolves according to the full Hamiltonian. This effect has important physical

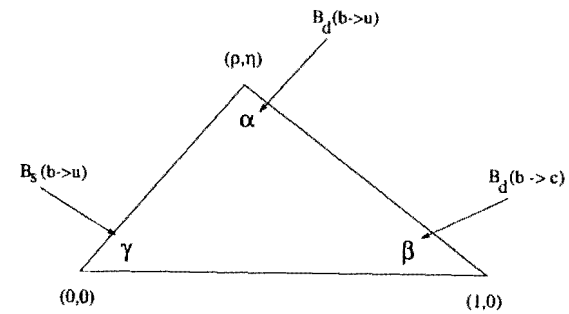

Figure A.1: *Geometrical representation of one of the relationships given by the unitarity of the CKM matrix. The transitions shown are the ones considered best suited to measure the corresponding angles. The decay mode $B_d \to J/\psi K_S^0$ can determine the angle β.*

consequences, one of them being that the usual exponential law for the decay of unstable particles does not apply for these systems.

In the B rest frame the time evolution is given by [19, Section VI.E]

$$i\frac{\partial}{\partial t}\begin{bmatrix} B^0 \\ \bar{B}^0 \end{bmatrix} = \mathcal{H}\begin{bmatrix} B^0 \\ \bar{B}^0 \end{bmatrix} \tag{A.17}$$

with $\mathcal{H}$ a 2×2 matrix representing an effective Hamiltonian having contributions from the strong and weak interactions. $\mathcal{H}$ is not hermitian as the states $B^0(\bar{B}^0)$ do decay. The eigenstates of $\mathcal{H}$ are written as [20]

$$\begin{aligned} |B_L> &= p|B^0> + q|\bar{B}^0> \\ |B_H> &= p|B^0> - q|\bar{B}^0> \end{aligned} \tag{A.18}$$

with H and L denoting the high and low mass state, p and q are functions of the elements of $\mathcal{H}$. The two states will have different masses and lifetimes. In the B_d^0 system the difference in lifetimes is supposed to be negligible.

By defining

$$\begin{aligned} M &\equiv \frac{M_H + M_L}{2} \\ \Delta M &\equiv M_H - M_L \\ \varphi_t &\equiv \frac{\Delta M t}{2} \end{aligned} \tag{A.19}$$

the proper time evolution of a state which is pure $B^0(\bar{B}^0)$ at $t = 0$ is given by

$$\begin{aligned} |B^0(t)> &= \exp(-\Gamma t/2)\exp(-iMt) \times \{\cos\varphi_t|B^0> + i\frac{q}{p}\sin\varphi_t|\bar{B}^0>\} \\ |\bar{B}^0(t)> &= \exp(-\Gamma t/2)\exp(-iMt) \times \{i\frac{p}{q}\sin\varphi_t|B^0> + \cos\varphi_t|\bar{B}^0>\} \end{aligned} \tag{A.20}$$

A.4 Classes of CP Violation

When computing decay amplitudes a distinction is made between the phases that arise from the CKM matrix (called weak phases) and phases arising from final state rescattering effects (called strong phases). The amplitude of the process $B \to f$ with f some final state is related to the amplitude of its CP conjugate process as

$$\begin{aligned} \mathcal{A}(B \to f) &= \sum_j A_j \exp(i(\delta_j + \phi_j)) \\ \bar{\mathcal{A}}(\bar{B} \to \bar{f}) &= \sum_j A_j \exp(i(\delta_j - \phi_j)) \end{aligned} \tag{A.21}$$

that is, the weak phases change sign and the strong phases remain unchanged.

Three classes of CP violating effects can be defined. Direct CP violation refers to a difference in the decay rates between the two processes in Eq. A.21 without any contribution from mixing effects. We can see that this requires at least 2 terms in the sum with different weak phases and different strong phases. CP violation via mixing refers to differences in the decay rate due to interference between the two paths shown in Fig. A.2. Indirect CP violation would arise from any difference in the lifetimes of the two eigenstates [20].

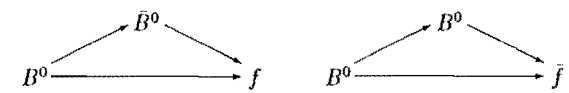

Figure A.2: *Two contributions to the total decay amplitude of a neutral B meson. The interference between them allows for differences in the decay rates of left diagram and right diagram.*

A.5 CP Violation in the $J/\psi K_S^0$ Mode

The decay mode $B_d \to J/\psi K_S^0$ is often referred as the "golden mode" for the study of CP violation in the B system. In this section we will show why this is so.

The first thing to know is that the $J/\psi K_S^0$ from a B_d decay is a CP eigenstate,

namely $CP|J/\psi K_S^0> = -|J/\psi K_S^0>$. This allows us to write the following relations for the decay rates of the states defined in Eq. A.20:

$$\begin{aligned}
\Gamma(B^0(t) \to f) &= \exp(-\Gamma t)|\mathcal{A}|^2 \times \\
&\quad \{\cos^2\varphi_t + \left|\frac{q\bar{\mathcal{A}}}{p\mathcal{A}}\right|^2 \sin^2\varphi_t + \mathrm{Im}\left(\frac{q\bar{\mathcal{A}}}{p\mathcal{A}}\right)\sin 2\varphi_t\} \\
\Gamma(\bar{B}^0(t) \to f) &= \exp(-\Gamma t)|\bar{\mathcal{A}}|^2 \times \\
&\quad \{\cos^2\varphi_t + \left|\frac{p\mathcal{A}}{q\bar{\mathcal{A}}}\right|^2 \sin^2\varphi_t + \mathrm{Im}\left(\frac{p\mathcal{A}}{q\bar{\mathcal{A}}}\right)\sin 2\varphi_t\} \qquad \text{(A.22)}
\end{aligned}$$

We make two approximations at this point. First we have neglected the effects of $\Delta\Gamma$; this can be shown to imply

$$\left|\frac{q}{p}\right| = 1 \qquad \text{(A.23)}$$

This decay mode can be shown to proceed mainly through the amplitude shown on the left of Fig. 1.1. From Eq. A.21 we can see this means

$$\frac{\mathcal{A}}{\bar{\mathcal{A}}} = \exp(2i\phi) \qquad \text{(A.24)}$$

in other words, the strong phase δ cancels and the ratio of amplitudes only depends on the weak phase ϕ.

With this simplifications we compute the asymmetry

$$\begin{aligned}
A_{CP} &\equiv \frac{\Gamma(B^0(t) \to f) - \Gamma(\bar{B}^0(t) \to \bar{f})}{\Gamma(B^0(t) \to f) + \Gamma(\bar{B}^0(t) \to \bar{f})} \\
&= \sin(\Delta M t)\mathrm{Im}\left(\frac{q\bar{\mathcal{A}}}{p\mathcal{A}}\right) \qquad \text{(A.25)}
\end{aligned}$$

By considering the box diagram and the diagram in Fig. 1.1 is possible to show that [19, Section X.F]

$$\frac{q\bar{\mathcal{A}}}{p\mathcal{A}} = \frac{V_{cd}^* V_{cs}}{V_{cd} V_{cs}^*}\frac{V_{cb} V_{cs}^*}{V_{cb}^* V_{cs}}\frac{V_{td} V_{tb}^*}{V_{td}^* V_{tb}} \qquad \text{(A.26)}$$

After some cancellations and using Eq. A.16 we find

$$A_{CP} = -\sin 2\beta \sin(\Delta M t) \qquad \text{(A.27)}$$

Appendix B

CDF TRACK MODEL

A set of formulas needed for this analysis are described here. We wrote several routines that implement them. Some of them are improvements over previously existing routines, others did not exist at the time.

The CDF track helixes are determined by the five parameters $c, \phi_0, \cot\theta, d_0$, and z_0. Definitions for these parameters can be found in the following text.

B.1 Derivation of Track Equations

From Fig. B.1 we can write the following expression for the point (x-y) at which the momentum is drawn (P^+ for a positive particle and P^- for a negative one)

$$\begin{aligned} x &= x_0 + |r|\cos\alpha \\ y &= y_0 + |r|\sin\alpha \end{aligned} \tag{B.1}$$

The angle α satisfies the following relations

$$\alpha = \phi^+ - \pi/2 = \phi^- - 3\pi/2 \tag{B.2}$$

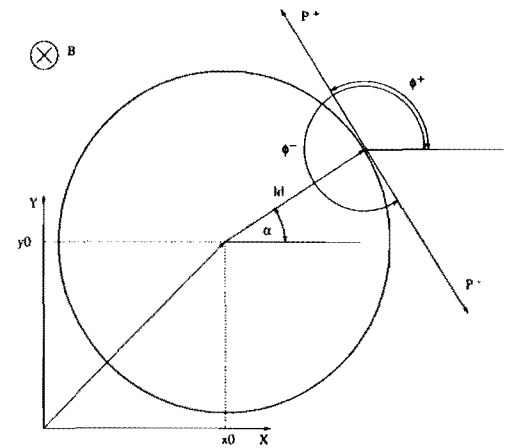

Figure B.1: *Track of a charged particle through CDF's magnetic field region.*

which implies that

$$\begin{aligned} \cos\alpha &= \sin\phi^+ = -\sin\phi^- = Q\sin\phi \\ \sin\alpha &= -\cos\phi^+ = \cos\phi^- = -Q\cos\phi \end{aligned} \tag{B.3}$$

where we define ϕ to be the polar angle for the momentum. If we define r to be the radius of the circle times the charge Q of the particle we get

$$\begin{aligned} x &= x_0 + r\sin\phi \\ y &= y_0 - r\cos\phi \end{aligned} \tag{B.4}$$

Following a similar kind of argument and defining $d \equiv \sqrt{x_0^2 + y_0^2} - |r|$ we can write the coordinates of the point of closest approach as

$$\begin{aligned} x_{CA} &= -dQ \sin \phi_0 \\ y_{CA} &= dQ \cos \phi_0 \end{aligned} \tag{B.5}$$

where ϕ_0 is defined to be the angle of the momentum at the point of closest approach. We can also use Eq. B.4 to get

$$\begin{aligned} x_{CA} &= x_0 + r \sin \phi_0 \\ y_{CA} &= y_0 - r \cos \phi_0 \end{aligned} \tag{B.6}$$

With the definition $d_0 \equiv Qd$ and by using Eq. B.5 and Eq. B.6 we find that

$$\begin{aligned} x_0 &= -(r + d_0) \sin \phi_0 \\ y_0 &= (r + d_0) \cos \phi_0 \end{aligned} \tag{B.7}$$

If we define s to be the arc length along the circle projected on the x-y plane by the particle's trajectory from the point of closest approach, we can write the following relation between s and the turning of the track momentum $\Delta\phi$

$$\Delta\phi = \frac{s}{r} \tag{B.8}$$

We can see that the momentum of positively charged particles turns in the direction of increasing polar angle while negative particles do the opposite. The angles ϕ

and ϕ_0 are related as

$$\phi = \phi_0 + \Delta\phi + 2n\pi \tag{B.9}$$

where n is an integer chosen to give ϕ in the range [0-2π] as is the CDF convention.

We finally write relations for the remaining two CDF track parameters c and $\cot\theta$

$$\begin{aligned} c &= \frac{1}{2r} \\ \cot\theta &= \frac{p_z}{p_t} \end{aligned} \tag{B.10}$$

We can then write the following relations:

$$\begin{aligned} x &= r \sin \phi - (r + d_0) \sin \phi_0 \\ y &= -r \cos \phi + (r + d_0) \cos \phi_0 \\ z &= z_0 + s \cot \theta \end{aligned} \tag{B.11}$$

B.2 Track Momentum at the Vertex

The CDF track parameters are given at the point of closest approach to the z axis of the global CDF coordinate system. For tracks produced by a long lived particle (like the $\pi^{\pm}$ tracks from a K_S^0) it is necessary to compute the momentum at the decay point $\vec{X_S}$. This is very simple to achieve. From the first two previous equations we get

$$\begin{aligned} \sin \phi &= \sin \phi_0 + \frac{X_S + d_0 \sin \phi_0}{r} \\ \cos \phi &= \cos \phi_0 + \frac{-Y_S + d_0 \cos \phi_0}{r} \end{aligned} \tag{B.12}$$

By definition ϕ is the angle of the tangent along the particle's trajectory. Then the momentum vector is obtained with

$$p_t = \frac{1.49896\mathrm{E}-4 \times B}{|c|} \tag{B.13}$$

$$\begin{aligned} p_x &= p_t \cos\phi \\ p_y &= p_t \sin\phi \\ p_z &= p_t \cot\theta \end{aligned} \tag{B.14}$$

where B is the magnetic field in KGauss.

B.3 Helix Parameters from GENP

Here we derive formulas that allow one to obtain the track equations for a particle of given momentum $\vec{P}$, created at the point $\vec{X}_V$, and with charge Q. We have implemented them in subroutine **XV_P_Q_HELIX**.

It is straightforward from Eq. B.13 to get

$$c = Q\frac{1.49896\mathrm{E}-4 \times B}{p_t} \tag{B.15}$$

and from Eq. B.14 we get

$$\cot\theta = \frac{p_z}{p_t} \tag{B.16}$$

We compute the coordinates of the center of the helix by using Eq. B.4

$$\begin{aligned} x_0 &= x_v - r\sin\phi \\ y_0 &= y_v + r\cos\phi \end{aligned} \tag{B.17}$$

where $\sin\phi$ and $\cos\phi$ are obtained with

$$\begin{aligned} \sin\phi &= \frac{p_y}{p_t} \\ \cos\phi &= \frac{p_x}{p_t} \end{aligned} \tag{B.18}$$

If we define $r_0 \equiv Q\sqrt{x_0^2 + y_0^2}$ we then have

$$d_0 = r_0 - r \tag{B.19}$$

As it stands, this formula is correct but numerically unstable. This is because $|d_0| \ll |r_0|$. To solve this problem we use a technique learnt from Joel Heinrich. We obtain an alternative expression for d_0 by multiplying Eq. B.19 by 1

$$d_0 = r_0 - r = \frac{(r_0 - r)(r_0 + r)/r}{(r_0 + r)/r} \equiv \frac{N}{D} \tag{B.20}$$

If we use Eq. B.17 we get

$$\begin{aligned} N &= (r_0 - r)(r_0 + r)/r \\ &= \frac{x_v^2 + y_v^2}{r} + 2(y_v\cos\phi - x_v\sin\phi) \\ D &= 1 + r_0/r \end{aligned} \tag{B.21}$$

We now obtain ϕ_0 by using the following relations from Eq. B.7 and Eq. B.19

$$\begin{aligned} \sin\phi_0 &= -\frac{x_0}{r_0} \\ \cos\phi_0 &= \frac{y_0}{r_0} \end{aligned} \tag{B.22}$$

We then use

$$\phi_0 = \text{cdfphi}\ (\text{atan2}\ (\sin\phi_0, \cos\phi_0)) \tag{B.23}$$

where **cdfphi** is the standard CDF routine which returns an angle between (0-2π).

Now we proceed to compute z_0. This is a bit more involved. We multiply the first line in Eq. B.11 by $\cos\phi_0$, the second line by $\sin\phi_0$ and add them we get

$$\sin(\frac{s}{r}) = \frac{x_v \cos\phi_0 + y_v \sin\phi_0}{r} \tag{B.24}$$

If we now multiply the first line by $\sin\phi_0$ and the second line by $\cos\phi_0$ and subtract it from the first one we get

$$\cos(\frac{s}{r}) = \frac{x_v \sin\phi_0 - y_v \cos\phi_0 + r_0}{r} \tag{B.25}$$

And finally we get

$$s = r \times \text{atan2}\ (\sin(\frac{s}{r}), \cos(\frac{s}{r})) \tag{B.26}$$

It must be pointed out that the solution provided is restricted to tracks that bend $< \pi$ from the point of closest approach to $\vec{X}_V$. For $p_t > 250$ MeV/c, this approximation is an excellent one. There is a simpler alternative to get s. We first compute the angle ϕ at $\vec{X}_V$

$$\phi_1 = \text{cdfphi}(\text{atan2}(p_y, p_x)) \tag{B.27}$$

we can then compute the bending as

$$\Delta\phi_{01} = \phi_1 - \phi_0 + 2k\pi \tag{B.28}$$

with k the integer that satisfies

$$|\phi_1 - \phi_0 + 2k\pi| < \pi \tag{B.29}$$

and we get for s

$$s = r\Delta\phi \tag{B.30}$$

Thus we get for z_0

$$z_0 = z_v - s\cot\theta \tag{B.31}$$

B.4 Exit Radius (R_E)

We want to compute the radius at which a helix exits the CTC. The formulas given here are implemented by routine **RADIUS**. There is no equivalent CDF routine to do this. The CDF routine **TRPROP** could be used with two consecutive calls to provide this result.

We first compute the turning a track undergoes to reach the CTC endplates. Let's define

$$z_M = \begin{cases} 150.0 & \text{if } \cot\theta > 0 \\ -150.0 & \text{if } \cot\theta < 0 \end{cases} \tag{B.32}$$

Let's first compute the radial distance to the origin as a function of the bending $\Delta\phi$. We take the first two lines from Eq. B.11 and compute

$$R_\phi = \sqrt{x^2 + y^2} = \sqrt{r^2 + (r + d_0)(r + d_0 - 2r\cos\Delta\phi)} \tag{B.33}$$

Using Eq. B.8 and bottom line in Eq. B.11 we find that the bending is given by

$$\Delta\phi = \frac{(z_M - z_0)}{r \cot\theta} \tag{B.34}$$

If $\Delta\phi < \pi$ that means the helix reaches the end of the CTC without turning inwards. Then we set

$$R_E = \sqrt{r^2 + (r + d_0)(r + d_0 - 2r\cos\Delta\phi)} \tag{B.35}$$

and if $R_E > R_{\rm CTC}$ we set $R_E = R_{\rm CTC}$.

If $\Delta\phi > \pi$ this means that the helix has turned inwards. There are two alternative situations. The most likely one is that the helix has exited the CTC through the sides at some point. The other possibility is that the particle turns inwards without exiting the CTC. This is very unlikely but we can handle it without much difficulty.

We compute the radius at the turning point by evaluating Eq. B.33 at $\Delta\phi = \pi$ to get

$$R_M = \sqrt{r^2 + (r + d_0)(d_0 + 3r)} \tag{B.36}$$

If $R_M < R_{\rm CTC}$ then we set

$$R_E = -R_M \tag{B.37}$$

We do this as the tracking code will reconstruct the inward and outward sections of the helix as two separate tracks. For the case of $R_M > R_{\rm CTC}$ we set

$$R_E = R_{\rm CTC} \tag{B.38}$$

B.5 Charged Particle Decay Vertex

We need to define 3 points for the helix associated with the particle. The point of closest approach to the origin, $\vec{X}_0$, the creation point $\vec{X}_1$, and the decay point $\vec{X}_2$.

We generate an exponential distribution for a particle with lifetime τ with

$$ct = -c\tau \log(u) \tag{B.39}$$

Here u is a random variable with uniform distribution $(0 - 1)$. The distance traveled by the particle in the laboratory reference frame is then

$$\begin{aligned} d &= \gamma\beta\, ct \\ &= \frac{P}{M}\, ct \end{aligned} \tag{B.40}$$

If we project both sides of the equation into the $(x\text{-}y)$ plane we get

$$d_T = \frac{P_T}{M}\, ct \tag{B.41}$$

Assuming that the particle does not leave the magnetic field region we compute the bending from $\vec{X}_1$ to $\vec{X}_2$ with

$$\Delta\phi_{12} = \frac{d_T}{r} \tag{B.42}$$

For very long lived particles this assumption will almost always be wrong, but we are only interested in particles that decay within the CTC. For particles decaying outside the CTC we will not compute the decay vertex.

We now compute the bending from $\vec{X}_0$ to $\vec{X}_1$. The reader must remember that in general, the particle may or may not go through $\vec{X}_0$. In CDF the general assumption is that the particle does not.

This is a good approximation, but there are cases when it is not correct. An example of possible situations is for particles coming from the beam and pointing towards the origin (the beam spot is displaced). This is a frequent situation but the error is small. It could also happen that a daughter from a long lived particle may move towards the origin. This will cause bigger errors but its an unlikely situation. Here we do not make this assumption. We first need to compute ϕ at $\vec{X}_1$

$$\phi_1 = \text{cdfphi}(\text{atan2}(Py, Px)) \tag{B.43}$$

We can then compute the bending as

$$\Delta\phi_{01} = \phi_1 - \phi_0 + 2k\pi \tag{B.44}$$

with k the integer that satisfies

$$|\phi_1 - \phi_0 + 2k\pi| < \pi \tag{B.45}$$

The implicit assumption is that the absolute value of the bending is $< \pi$. This is an excellent assumption for CDF. We can now compute the total bending from $\vec{X}_0$ to $\vec{X}_2$ with

$$\Delta\phi_{02} = \Delta\phi_{12} + \Delta\phi_{01} \tag{B.46}$$

If $|\Delta\phi_{02}| > \pi$, that means the helix turns inward. We are not worried about the inward portion of the helix so we set $|\Delta\phi_{02}| = \pi$. We now compute the decay radius of the particle with

$$R_D = \sqrt{r^2 + (r + d_0)(r + d_0 - 2r\cos\Delta\phi_{02})} \tag{B.47}$$

We can now decide whether the particle decays inside the CTC or not. For the case $R_D <= R_E$ the particle has decayed inside and we then compute the decay vertex using formulas B.11 with

$$\phi = \phi_0 + \Delta\phi_{02} \tag{B.48}$$

plus the arc length given by

$$s_{02} = \Delta\phi_{02} \times r \tag{B.49}$$

Appendix C

ROTATING A VECTOR

We want to find the linear transformation that rotates a vector $\vec{p}_1$ into a vector $\vec{p}_2$. It is possible to obtain the transformation as a matrix that is related to the Euler angles. For this note we will derive a simpler formulation valid only for 3 dimensions. The formulas developed here are implemented in subroutine **ROTATE**.

Let's define $\hat{n}$ to be a unitary vector perpendicular to the plane defined by $\vec{p}_1$ and $\vec{p}_2$

$$\hat{n} = \frac{\vec{p}_1 \times \vec{p}_2}{|\vec{p}_1 \times \vec{p}_2|} \tag{C.1}$$

We can now restate the problem as finding the linear transformation that rotates any vector around $\hat{n}$ by an angle α given by

$$\begin{aligned} \sin\alpha &= \frac{|\vec{p}_1 \times \vec{p}_2|}{|\vec{p}_1||\vec{p}_2|} \\ \cos\alpha &= \frac{\vec{p}_1 \cdot \vec{p}_2}{|\vec{p}_1||\vec{p}_2|} \end{aligned} \tag{C.2}$$

These expressions define α in the range $(0\text{-}\pi)$.

A general vector $\vec{v}$ is more conveniently expressed as $\vec{v} = \vec{v}_\parallel + \vec{v}_\perp$ with respect to $\hat{n}$. Then a rotation around $\hat{n}$ leaves $\vec{v}_\parallel$ unchanged. All we need to worry about is the transformation of $\vec{v}_\perp$.

For $0 < \alpha < \pi/2$, $\vec{v}'_\perp$ will be along the unitary vector

$$\hat{u} = \frac{\vec{v}_\perp + \hat{n} \times \vec{v}_\perp \tan\alpha}{|\vec{v}_\perp|\sqrt{1+\tan^2\alpha}} \tag{C.3}$$

To verify this assertion the reader can check that $\hat{u} \cdot \vec{v}_\perp / |\vec{v}_\perp| = |\cos\alpha| = \cos\alpha$ for the range of α under consideration.

For $\pi/2 < \alpha < \pi$ the reader can verify that $\vec{v}'_\perp$ will be along $-\hat{u}$ by realizing that $-\hat{u} \cdot \vec{v}_\perp / |\vec{v}_\perp| = -|\cos\alpha| = \cos\alpha$ for the range of α under consideration.

Finally we can write

$$\vec{v}'_\perp = \frac{\tan\alpha}{|\tan\alpha|}|\vec{v}_\perp|\,\hat{u} \tag{C.4}$$

Using the expressions $\vec{v}_\parallel = (\vec{v}\cdot\hat{n})\,\hat{n}$, $\vec{v}_\perp = \vec{v} - \vec{v}_\parallel$ and by realizing that $\hat{n} \times \vec{v}_\perp = \hat{n} \times \vec{v}$ we can write

$$\vec{v}'_\perp = \frac{\tan\alpha}{|\tan\alpha|}\,\frac{\vec{v} - (\vec{v}\cdot\hat{n})\hat{n} + \tan\alpha\,\hat{n} \times \vec{v}}{\sqrt{1+\tan^2\alpha}} \tag{C.5}$$

Finally we have the following expression for the rotated vector $\vec{v}'$

$$\tan\alpha = \frac{|\vec{p}_1 \times \vec{p}_2|}{\vec{p}_1 \cdot \vec{p}_2}$$

$$\vec{v}' = (\vec{v}\cdot\hat{n})\hat{n} + \frac{\tan\alpha}{|\tan\alpha|}\frac{\vec{v} - (\vec{v}\cdot\hat{n})\hat{n} + \tan\alpha\,\hat{n}\times\vec{v}}{\sqrt{1+\tan^2\alpha}} \qquad \text{(C.6)}$$

Bibliography

[1] O. Nachtmann, *Elementary Particle Physics*, Springer-Verlag (1990)

[2] Ikaros Bigi *et al.*, *Non-Leptonic Decays of Beauty Hadrons-from Phenomenology to Theory*, in B Decays, ed. Sheldon Stone, World Scientific 1994.

[3] **CLEO** collaboration, *Exclusive Hadronic B Decays to Charm and Charmonium Final States*, CLNS 94-1270, CLEO 95-5 (accessible via www)

[4] F. Abe *et al.*, *A Measurement of the B Meson and b-quark Cross Section at* $\sqrt{s} = 1.8$ *Tev Using the Exclusive Decay* $B^{\pm} \to J/\psi K^{\pm}$ Phys. Rev. Lett. 68 (1992) 3403

[5] Marina Artuso, *Experimental Facilities for b-quark Physics*, in B Decays, ed. Sheldon Stone, World Scientific 1994.

[6] CDF collaboration, *Measurement of the* B^+ *and* B^0 *Lifetimes*, Phys. Rev. Lett. 72 (1994) 3456

[7] Ahmed Ali, em b Decays - Introduction and Overview, in B Decays, ed. Sheldon Stone, World Scientific 1994.

[8] Feynman diagrams were drawn with **FeynDiagram** version 2.2, written by Bill Dimm and available via anonymous **FTP** from 128.84.251.21

[9] Donald H. Perkins, *Introduction to High Energy Physics*, Addison-Wesley 1982.

[10] M. Bauer, B. Stech and M. Wirbel, *Exclusive Non-Leptonic Decays of D-, D_s- and B-Mesons*, Z. Phys. C 34 (1987) 103

[11] Thomas Browder and Klaus Honscheid, *B Mesons*, hep-ph/9503414. The postscript version (incl. figures) as well as the uuencoded version (incl figures) are available via anonymous ftp at ftp://pacific.mps.ohio-state.edu/pub/hepex/kh as the files breview.ps and breview.uu

[12] M. Gourdin, A. Kamal and X. Pham, *Difficulties in Explaining Recent Data on $B \to J/\psi K(K^*)$ Decays with Commonly Used Form Factors within the Factorization Approach*, Phys. Rev. Lett. 73 (1994) 3355

[13] K. Ohl, *Measurement of the Polarization in the Decay $B^0 \to J/\psi K^{*0}$ in $\bar{p}p$ Collisions at $\sqrt{s} = 1.8$ TeV*, submitted to the Eighth Meeting of the Division of Particles and Fields of the American Physical Society (DPF '94), Albuquerque, New Mexico, August 2-6, 1994. Available at http://www-cdf.fnal.gov/physics/conf94/conf94.html

[14] J. Cristenson, J. Cronin, V. Fitch and R. Turlay, Phys. Rev. Lett. 13 (1964) 138

[15] B. Winstein and L. Wolfenstein, *The Search for Direct CP Violation*, Rev. Mod. Phys. 65 (1993) 1113

[16] Y. Nir, *New Physics Effects on CP Violation in B Decays*, in Proceedings of the Workshop on B Physics at Hadron Accelerators, Snowmass 1993, ed. P. McBride, C. Mishra.

[17] T. Cheng and L. Li, *Gauge Theory of Elementary Particle Physics*, Oxford University Press 1989

[18] P. Langacker, *Grand Unified Theories and Proton Decay*, Phys. Reports 72, No.4(1981) 185

[19] J. Rosner, *Heavy Quarks, Quark Mixing, and CP Violation*, in Testing the Standard Model, ed. M. Cvetič and P. Langacker, World Scientific 1991

[20] H. Quinn, *$B^0 - \bar{B}^0$ Mixing and CP Violation in B Decay*, Phys. Rev. D 50 (1994) 1632.

[21] M. Gronau, *CP Violation in the Standard Model: the B Meson System* in Proceedings of the Workshop on B Physics at Hadron Accelerators, Snowmass 1993, ed. P. McBride, C. Mishra.

[22] F. Abe *et al.*, Nucl. Instr. and Meth., Sect. A271(1988) 387.

[23] Fermilab World Wide Webb home page, http://fnnews.fnal.gov/fermilab_home .html

[24] William Wester, *A Measurement of the Mass of the B_s^0 Meson in Proton- Antiproton Collisions at $\sqrt{s} = 1.8$ Tev* , Ph.D. Thesis, 1994

[25] F. BEDESCHI *et al.*, Nucl. Instr. and Meth., Sect. A228(1988) 50.

[26] Mark Bailey, *Measurement of the b Quark and B Meson Cross-Sections in Proton-Antiproton Collisions at 1.8 Tev Using Fully Reconstructed Decays*, Ph.D. Thesis, 1994

[27] D. Amidei *et al.*, *The Silicon Vertex Detector of the Collider Detector at Fermilab*, Nucl. Instr. and Meth., Sect. A350(1994) 73.

[28] G. Ascoli *et al.*, *CDF Central Muon Level-1 Trigger Electronics*, Nucl. Instr. and Meth., Sect. A269(1988) 63.

[29] R. Bock *et al.*, *Data Analysis Techniques for High-Energy Physics Experiments*, Cambridge University Press (1990)

[30] A. Mukherjee, Internal Communication.

[31] P. Berge, Internal Communication.

[32] Mark Bailey *et al.*, *CTC Tracking Efficiency for the B Cross-Section Analysis*, CDF note 2815.

[33] Julio González *et al.*, *Measurement of CTC Tracking Efficiency, Offline Version 7_09, for $B^\pm \to J/\psi K^\pm$, $B^0 \to J/\psi K_S^0$ and $B^\pm \to J/\psi K^{*\pm}$* , CDF note 3010

[34] Hans Wenzel, *Tracking in the SVX*, CDF note 1790

[35] Hans Wenzel *et al.*, *Update on the Inclusive B-Lifetime Measurement*, CDF note 2062

[36] Julio González *et al.*, *Improved K_S^0 Reconstruction Using the SVX*, CDF note 2277

[37] Weiming Yao *et al.*, *Top Search in Lepton+ Jets Using SVX with Improved Tracking*, CDF note 2072

[38] Richard Hughes, *Reconstruction of B Meson Decays and Measurement of the b Quark and B Meson Production Cross Sections at the Fermilab Tevatron Collider*, Ph.D. Thesis, 1992. Also *A Measurement of the B Meson and b-quark Cross-Sections at $\sqrt{s} = 1.8$ TeV Using the Exclusive Decay $B^\pm \to J/\psi K^\pm$*, Phys. Rev. Lett., 68 (1992) 3403

[39] I. Dunietz and J. Rosner, *Isospin Considerations in Correlations of Pions and B Mesons*, FERMILAB-PUB-94/298-T, hep-ph/9411213

[40] Hans Wenzel *et al.*, *Measurement of the B Lifetime with Inclusive Ψ's at CDF*, CDF note 1933; Phys. Rev. Lett. 71 (1993) 3421

[41] V. Papadimitriou *et al.*, *$J/\psi, \psi' \to \mu^+\mu^-$ and $B \to J/\psi, \psi'$ Cross Sections*, CDF note 2599

[42] Randal Hans *et al.*, *Helicity Analysis of $B^0 \to J/\psi K^*$*, CDF note 2941

[43] Randal Hans *et al.*, *Level 1 and Level 2 Low P_T Central Muon Trigger Efficiencies for Run Run-Ia*, CDF note 1999

[44] Troy Daniels, internal communication.

[45] M. Saulnier, *Semileptonic Decays of B Mesons*, TALK94-14

[46] OPAL collaboration, *Improved Measurements of the B^0 and B^+ Meson Lifetimes* CERN-PPE/95-019, to be submitted to Zeit. f. Physic C

[47] DELPHI collaboration, *Lifetimes of Charged and Neutral B Hadrons Using Event Topology*, CERN-PPE/95-59, to be submitted to Zeit. f. Physic C

[48] DELPHI collaboration, *A Measurement of B^+ and B^0 Lifetimes using $\bar{D}l^+$ Events*, CERN-PPE/95-60, to be submitted to Zeit. f. Physic C

[49] F. Ukegawa *et al.*, *Updated Measurement of the B Meson Lifetimes Using Semileptonic Decays*, CDF note 3009

[50] Particle Data Group, *Review of Particle Properties*, Phys. Rev. D. 50 (1994)

[51] H. Yamamoto, *B Decays-Measurements and Predictions*, in Proceedings of the Workshop on B Physics at Hadron Accelerators, Snowmass 1993, ed. P. McBride, C. Mishra.

[52] R. Peccei, Summary Talk, The Third KEK Topical Conference on CP Violation (1993).